



HAL
open science

Analysis of Titan CH 3.3 μm upper atmospheric emission as measured by Cassini/VIMS

Maya García-Comas, Manuel López-Puertas, Bernd Funke, Bianca M. Dinelli, Maria Luisa Moriconi, Alberto Adriani, Antonio Molina, Angioletta Coradini

► **To cite this version:**

Maya García-Comas, Manuel López-Puertas, Bernd Funke, Bianca M. Dinelli, Maria Luisa Moriconi, et al.. Analysis of Titan CH 3.3 μm upper atmospheric emission as measured by Cassini/VIMS. *Icarus*, 2011, 214 (2), pp.571. 10.1016/j.icarus.2011.03.020 . hal-00786867

HAL Id: hal-00786867

<https://hal.science/hal-00786867>

Submitted on 11 Feb 2013

HAL is a multi-disciplinary open access archive for the deposit and dissemination of scientific research documents, whether they are published or not. The documents may come from teaching and research institutions in France or abroad, or from public or private research centers.

L'archive ouverte pluridisciplinaire **HAL**, est destinée au dépôt et à la diffusion de documents scientifiques de niveau recherche, publiés ou non, émanant des établissements d'enseignement et de recherche français ou étrangers, des laboratoires publics ou privés.

Accepted Manuscript

Analysis of Titan CH₄ 3.3 μm upper atmospheric emission as measured by Cassini/VIMS

Maya García-Comas, Manuel López-Puertas, Bernd Funke, Bianca M. Dinelli, Maria Luisa Moriconi, Alberto Adriani, Antonio Molina, Angioletta Coradini

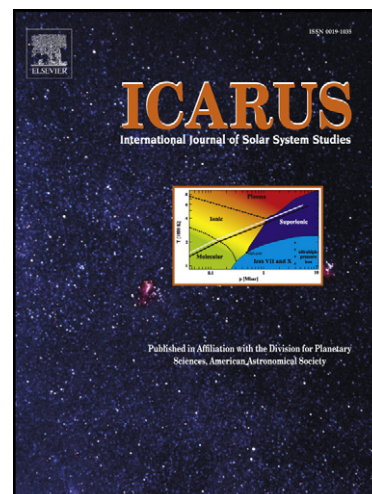
PII: S0019-1035(11)00111-4
DOI: [10.1016/j.icarus.2011.03.020](https://doi.org/10.1016/j.icarus.2011.03.020)
Reference: YICAR 9763

To appear in: *Icarus*

Received Date: 3 December 2010
Revised Date: 21 March 2011
Accepted Date: 23 March 2011

Please cite this article as: García-Comas, M., López-Puertas, M., Funke, B., Dinelli, B.M., Moriconi, M.L., Adriani, A., Molina, A., Coradini, A., Analysis of Titan CH₄ 3.3 μm upper atmospheric emission as measured by Cassini/VIMS, *Icarus* (2011), doi: [10.1016/j.icarus.2011.03.020](https://doi.org/10.1016/j.icarus.2011.03.020)

This is a PDF file of an unedited manuscript that has been accepted for publication. As a service to our customers we are providing this early version of the manuscript. The manuscript will undergo copyediting, typesetting, and review of the resulting proof before it is published in its final form. Please note that during the production process errors may be discovered which could affect the content, and all legal disclaimers that apply to the journal pertain.



**Analysis of Titan CH₄ 3.3 μ m upper
atmospheric emission as measured by
Cassini/VIMS**

Maya García-Comas^a Manuel López-Puertas^a Bernd Funke^a

Bianca M. Dinelli^b Maria Luisa Moriconi^c Alberto Adriani^d

Antonio Molina^{a,e} Angioletta Coradini^d

^a*Instituto de Astrofísica de Andalucía-CSIC, Glorieta de la Astronomía s/n,
18008 Granada, Spain*

^b*ISAC-CNR, Via Gobetti 101, 40129 Bologna, Italy*

^c*ISAC-CNR, Via Fosso del Cavaliere, 100, 00133 Roma, Italy*

^d*INAF-IFSI, Via Fosso del Cavaliere, 100, 00133 Roma, Italy*

^e*Dpto. Física Aplicada-Universidad de Granada, Fuentenueva s/n, 18071
Granada, Spain*

Abstract

After molecular nitrogen, methane is the most abundant species in Titan's atmosphere and plays a major role in its energy budget and its chemistry. Methane has strong bands at 3.3 μ m emitting mainly at daytime after absorption of solar radiation. This emission is strongly affected by non-local thermodynamic equilibrium (non-LTE) in Titan's upper atmosphere and, hence, an accurate modeling of the non-LTE populations of the emitting vibrational levels is necessary for its analysis. We present a sophisticated and extensive non-LTE model which considers 22 CH₄

levels and takes into account all known excitation mechanisms in which they take part. Solar absorption is the major excitation process controlling the population of the ν_3 -quanta levels above 1000 km whereas the distribution of the vibrational energy within levels of similar energy through collisions with N_2 is also of importance below that altitude. CH_4 - CH_4 vibrational exchange of ν_4 -quanta affects their population below 500 km. We found that the ν_3 -ground band dominates Titan's 3.3 μm daytime limb radiance above 750 km whereas the $\nu_3+\nu_4 \rightarrow \nu_4$ band does below that altitude and down to 300 km. The $\nu_3+\nu_2 \rightarrow \nu_2$, the $2\nu_3 \rightarrow \nu_3$, and the $^{13}CH_4$ ν_3 -ground bands each contribute from 5 to 8% at regions below 800 km. The $\nu_3+2\nu_4 \rightarrow 2\nu_4$ and $\nu_2+\nu_3+\nu_4 \rightarrow \nu_2+\nu_4$ bands each contribute from 2 to 5% below 650 km. Contributions from other CH_4 bands are negligible. We have used the non-LTE model to retrieve the CH_4 abundance from 500 to 1100 km in the southern hemisphere from Cassini-VIMS daytime measurements near 3.3 μm . Our retrievals show good agreement with previous measurements and model results, supporting a weak deviation from well mixed values from the lower atmosphere up to 1000 km.

Key words: Titan, Infrared, Observations, CH_4 , non-LTE,

1 Introduction

1 The absorption of solar radiation in the CH_4 vibrational bands in the near-
 2 infrared (mainly between 1 and 3.5 μm) plays a major role in the thermal
 3 balance of Titan upper atmosphere (Appleby, 1990; Yelle, 1991). Thus, its
 4 accurate modeling is very important for establishing its thermospheric tem-
 5 perature structure.

6 Measurements of CH_4 3.3 μm emissions of Titan upper atmosphere have been
 7 taken from Earth-based observations in the recent past (Kim et al., 2000;

9 tral resolution, their vertical and horizontal resolution is rather poor. In addi-
10 tion, the strong telluric absorptions affecting many lines make it difficult to
11 quantitatively assess the contributions of some bands. Kim et al. (2000) were
12 able to discriminate between the strongest $\nu_3 \rightarrow$ ground fundamental band and
13 the weaker $\nu_3 + \nu_4 \rightarrow \nu_4$ transition, showing, in spite of the large difference in
14 strength, comparable intensities. They found that the nadir emission from Ti-
15 tan in these bands originates at 530–630 km. They, however, were not able
16 to observe any other weak band contributing in this spectral region, e.g.,
17 the $2\nu_3 \rightarrow \nu_3$ or $\nu_2 + \nu_3 \rightarrow \nu_2$. By using a simplified non-LTE model, they de-
18 rived collisional de-excitation rates for the ν_3 and $\nu_3 + \nu_4$ levels, being smaller
19 for the latter, and made an estimation of the temperature of ~ 140 K in the
20 ~ 400 – 700 km altitudes. Geballe et al. (2003) also observed Titan’s atmosphere
21 from ground-based instrumentation with high spectral resolution in the 2.9–
22 $3.5 \mu\text{m}$ region. They observed the CH_4 $\nu_3 + \nu_4 \rightarrow \nu_4$ and $\nu_3 + \nu_2 \rightarrow \nu_2$ bands, and
23 the $\nu_3 \rightarrow$ ground HCN emission near $3.0 \mu\text{m}$, and claimed that they originated
24 in the upper atmosphere. They were able to account for the methane emission
25 around the mesopause (using the abundances derived by Kim et al. (2000),
26 i.e., 1.9%) but they needed an abundance around the mesopause about three
27 orders of magnitude larger than the accepted values to reproduce the HCN
28 emission,. Later re-analysis of that data (Yelle and Griffith, 2003; Kim et al.,
29 2005) revealed that the HCN emission measured mainly originated at signif-
30 icantly lower altitudes (300–400 km) and that accepted values of HCN were
31 actually able to account for the emission. Also Seo et al. (2009) analyzed the
32 same measurements, although limited to the 2.87– $3.12 \mu\text{m}$ region. They de-
33 rived from observations around $3.1 \mu\text{m}$ (tropospheric) methane mixing ratios
34 consistent with the Gas Chromatograph Mass Spectrometer (GCMS) mea-

35 surements (Niemann et al., 2005) within a factor of two, at least at low and
36 mid-latitudes. Negrão et al. (2006) successfully modeled the CH_4 absorption in
37 the 1–2.5 μm region measured by a mid-spectral resolution ground-based spec-
38 trometer assuming a constant mixing ratio of 1.8% above the tropopause. The
39 ISO Earth-orbiting observatory also performed observations of Titan’s near-
40 infrared atmospheric bands, mainly from methane. The analysis of Coustenis
41 et al. (2006) shows that ISO’s highest altitude probed at 3.3 μm is around
42 200 km whereas it is about 120 km for shorter wavelengths. They derived CH_4
43 disk-averaged abundances at the surface not exceeding 3%.

44 More recently, observations of Titan atmosphere in this spectral region have
45 been taken by the Cassini Visual-Infrared Mapping Spectrometer (VIMS) dur-
46 ing the several encounters of the Cassini spacecraft with Titan since late 2004
47 until present. These observations offer an unprecedented opportunity to study
48 the middle and upper atmosphere of Titan, since the spectra show a wealth of
49 near-infrared emissions, including those of HCN (Adriani et al., 2011), CH_4 ,
50 CH_3D , C_2H_2 , and CO (Baines et al., 2005, 2006). A preliminary analysis of
51 some of the observations in the CH_4 3.3 μm region has been presented by
52 Brown et al. (2006). They described the major features of the CH_4 emis-
53 sion in this spectral region and deduced a CH_4 volume mixing ratio in the
54 stratosphere of 0.02, although with a rather large uncertainty (50%).

55 In this paper, we study the Cassini/VIMS 3.3 μm emissions in Titan’s mesosphere
56 and thermosphere in more detail. We used spectra collected from tangent al-
57 titudes, that is, emission measured at the limb (almost perpendicular to the
58 surface), to better resolve the vertical structure. The major emitter in this
59 spectral region is CH_4 which, because of its large abundance and its rich vi-
60 brational spectra, has many weak and strong bands that contribute to these

61 Titan's limb near-infrared emissions. We have developed a sophisticated non-
62 LTE model, based on our previous model for CH₄ and other gases on the
63 Earth's atmosphere (López-Puertas and Taylor, 2001; Funke et al., 2007),
64 which calculates the populations of the CH₄ vibrational levels. The model was
65 adapted to Titan atmospheric conditions and a thorough study of the radia-
66 tive processes and collisional mechanisms involved has been carried out. This
67 allowed us to analyze in detail the sources of excitation of CH₄ emission from
68 500 to 1100 km of Titan and, specifically, to quantify the contributions of the
69 different, strong and weak, CH₄ bands to the atmospheric limb radiance. We
70 have used the non-LTE model to derive the CH₄ abundance in Titan upper at-
71 mosphere (500–1100 km) from VIMS daytime measurements near 3.3 μm and
72 to address the constraints imposed by the uncertainties in the non-LTE model
73 parameters.

74 2 Observational Data

75 The Visual-Infrared Mapping Spectrometer (VIMS) on board the Cassini
76 spacecraft is an imaging spectrometer capable of obtaining data cubes with up
77 to 64 \times 64 pixels in the spatial field of view, and 352 separate wavelengths for
78 each of these pixels. The angular resolution varies from 0.17 \times 0.17 mrad over
79 the visual (VIS) channel (0.35–1.08 μm) to 0.25 \times 0.5 mrad over the infrared
80 (IR) channel (0.85–5.2 μm). The visible-wavelength portion of the data cube
81 is provided by a frame-transfer CCD. The infrared spectrum beyond 0.9 μm
82 is provided by a single linear array of 256 InSb photo detectors with constant
83 0.12 mm spacing. The VIMS optics includes a tip/tilt mirror that step-scans
84 the image plane over the entrance aperture of the IR spectrometer. The VIS

85 and IR channels have spectral resolutions of 7 nm and 16 nm, respectively.

86 More details on the instrument can be found in Brown et al. (2004). In this
87 paper we analyze only the spectral region around 3.3 μm taken in the IR
88 channel, where the spectral resolution is ~ 16 nm.

89 The Cassini spacecraft has visited Titan 45 times during its nominal mission
90 (last flyby, T44, on 28th May 2008) since its arrival at the Saturn system in
91 the fall of 2004. From those measurements, we analyze in this paper the data
92 taken during two flybys: T34 (19 July 2007) and T35 (31 August 2007) (see
93 Table 1).

94 The calibration (both spectral and radiometric) of the images has been carried
95 out using the last updated VIMS pipeline (RC17), as described in McCord
96 et al. (2004), Filacchione (2006), Filacchione et al. (2007), and Clark et al.
97 (2010). The instrument noise error in the 3.3 μm region is about $3 \times 10^{-8} \text{ W m}^{-2} \text{ nm}^{-1} \text{ sr}^{-1}$.
98 Regarding the spectral calibration, VIMS IR wavelength values vary linearly
99 with the band number, following the expression $\lambda = 0.01668 \times B - 0.7381 \mu\text{m}$
100 where $B=96-351$ for the IR channel. Only a small but clear pattern deviation
101 from that linear fit occurs, which is smaller than 0.1% in the region around
102 3.3 μm (Cruikshank et al., 2009).

103 The geometry of the observations (latitude, longitude, distance from the space-
104 craft, local time, and phase, emission and incidence angles for each centre pixel
105 for every cube) has been determined using an *ad hoc* NAIF-SPICE toolkit (Ac-
106 ton, 1996) that takes into account the VIMS navigation parameters reported
107 in each PDS header taking into account the specific parameters of the VIMS
108 instrument. For each cube, we have collected all the available spectra at tan-
109 gent altitudes ranging from around 500 to 1200 km. In order to assure the

110 selection of profiles normal to the surface, we have selected the pixels covering
111 the atmosphere with geographical coordinates such that they differ less than
112 1° from those of the corresponding pixel at the surface (see Adriani et al.
113 (2011) for further details). The coordinates of the tangent height profiles for
114 all cubes analyzed here are listed in Table 1 and plotted in Fig. 1.

115 We have selected the spectral cubes attending the following criteria. First,
116 since we are interested in the high altitude region (above 400–500 km), where
117 the atmospheric signal is weak, we have selected those cubes with the smallest
118 noise, that is, the largest integration time. Secondly, we selected spectral cubes
119 covering as large as possible a latitudinal range. Thirdly, we tried to have
120 the best vertical resolution as possible, better than ~ 100 km. Finally, we
121 selected spectral cubes characterized by a phase angle lower than 60° both to
122 minimize the stray-light contamination and to have the largest atmospheric
123 signal. Since the emissions we analyzed are excited by absorption of solar
124 radiation, the highest the Sun over the horizon (smaller solar zenith angle,
125 SZA), the largest the expected signal. We stress that daytime measurements
126 during the flybys analyzed are limited to the southern hemisphere and so are
127 the retrieved CH_4 abundances derived in this study. Measurements covering
128 the northern hemisphere were taken during nighttime, where the non-LTE
129 emission vanishes.

131 *3.1 Description of the non-LTE model*

132 We have adapted the Generic RAdiative traNsfer AnD non-LTE popula-
133 tion Algorithm (GRANADA) non-LTE code (described in more detail in
134 Funke et al. (2009)) to calculate the CH₄ vibrational temperatures for Ti-
135 tan’s atmosphere. That model was originally developed for the Earth’s at-
136 mosphere and uses a generalized scheme for inclusion of radiative and colli-
137 sional processes for calculating the populations of any specified molecule. The
138 line-by-line radiative transfer calculations within GRANADA are performed
139 with the Karlsruhe Optimized and Precise Radiative transfer Algorithm (KO-
140 PRA) (Stiller et al., 2002).

141 The CH₄ molecule has four fundamental modes of vibration: two bending
142 modes (the symmetric v_2 and the asymmetric v_4) and two stretching modes
143 (the symmetric v_1 and the asymmetric v_3). We will note hereafter the vibra-
144 tional levels as (v_1, v_2, v_3, v_4) or, for simplicity, $v_1\nu_1 + v_2\nu_2 + v_3\nu_3 + v_4\nu_4$. Both
145 refer to levels with a total of v_1, v_2, v_3 and v_4 quanta in the v_1, v_2, v_3 and v_4
146 modes, respectively. That way, for example, level (0,0,1,2) will also be noted
147 as $\nu_3 + 2\nu_4$.

148 We consider eighteen vibrational levels of the main isotope ¹²CH₄ and 4 levels
149 of the second most abundant isotope ¹³CH₄, including their ground levels (see
150 Table 2). Figure 2 shows the energy levels included for the main isotope, that
151 are grouped in “equivalent” levels which have similar energies and therefore
152 are expected to suffer similar collisional processes. Each of these groups is

153 noted hereafter as V^* , where $*$ =7.6, 3.3, 2.3 and 2.7 refers to the approximate
154 wavelength corresponding to the mean energy of the levels in the group. It
155 is important to note that, even if we define these groups, we treat each of
156 their levels separately in the non-LTE modeling. We include as well forty-
157 one vibrational bands (see Table 3), out of which radiative transfer between
158 atmospheric layers is calculated for twenty-two.

159 The inversion of the system of multilevel steady state equations has been per-
160 formed with GRANADA using the Curtis matrix formalism (López-Puertas
161 and Taylor, 2001). GRANADA has also the ability to solve the system us-
162 ing the lambda iteration method. We chose the Curtis matrix formalism be-
163 cause it showed a similar accuracy and it is less computationally expensive.
164 The spectroscopic data were taken from the HITRAN compilation, 2004 edi-
165 tion (Rothman et al., 2005) with the addition of data for bands $2\nu_3 \rightarrow \nu_3$,
166 $\nu_2 + \nu_3 + \nu_4 \rightarrow \nu_2 + \nu_4$, $\nu_3 + 2\nu_4 \rightarrow 2\nu_4$, and $4\nu_4 \rightarrow 2\nu_4$ (Wenger and Champion (1998);
167 V. Boudon, private communication, 2009). The solar fluxes have been adapted
168 from SOLAR 2000 (Tobiska et al., 2000), considering the Sun-Saturn distance.

169 The collisional processes included in our model are listed in Table 4. These
170 processes connect the levels as shown in Fig. 2. Briefly, processes 1a, 1b, 2a
171 and 2b include the thermal relaxation of the bending modes ν_2 and ν_4 in
172 collisions with N_2 and CH_4 . The most effective of them are collisions between
173 the most abundant N_2 with methane molecules excited in the asymmetric
174 bending mode ν_4 (process 1a). Processes 3a and 3b account for the vibrational-
175 thermal, V-T, collisional re-distribution of vibrational quanta among the levels
176 in a given group. The latter also take place mainly in collisions with N_2 (process
177 3a). Processes 4, 5, and 6 describe the vibrational-vibrational (V-V) coupling
178 between CH_4 levels exchanging ν_4 , ν_2 , and ν_3 quanta, respectively. The most

179 important of these processes affecting the population of the levels are processes
 180 1a, 3a and 4. Process 1a keeps the levels in or close to local thermodynamic
 181 equilibrium (LTE), all levels in each group are coupled to each other through
 182 the fast thermal collisions with the abundant N_2 (process 3a), and each group
 183 is connected to the group with closest energy below mainly through ν_4 -quanta
 184 exchange (process 4). The latter also couples levels excited in the ν_4 mode
 185 ($\nu_4 > 1$) to the ν_4 level ($\nu_4 = 1$). The rest of the processes have little effect on
 186 the vibrational populations.

187 Figure 3 shows the vibrational temperatures of the CH_4 levels of the main
 188 isotope. The vibrational temperature of a vibrational level v is widely used to
 189 describe its non-LTE population and is defined as:

$$190 \quad T_v = -\frac{E_v}{k \ln\left(\frac{n_v g_0}{n_0 g_v}\right)}, \quad (1)$$

191 where n_v and n_0 are the number density of the vibrational level v and the
 192 ground vibrational state, respectively, and g_v and g_0 their degeneracies. E_v
 193 is the energy of level v , and k is the Boltzmann constant. The pressure-
 194 temperature (p-T) profile used is a composition of the Titan's atmosphere
 195 engineering model of Yelle et al. (1997) below 480 km, scaled to Huygens At-
 196 mospheric Structure Instrument (HASI) measurements (Fulchignoni et al.,
 197 2005), and the HASI results above that altitude (hereafter YH-atmosphere).
 198 We smoothed the HASI profile and kept it constant for altitudes higher than
 199 650 km in order to remove the potential effect of dynamics on the thermal
 200 structure. The N_2 number densities are those derived from the Huygens probe's
 201 GCMS measurements (Niemann et al., 2005) (freely accessible from <http://pds-atmospheres.nmsu.edu>) below 500 km and Cassini's Ion Neutral Mass Spec-
 202 trometer (INMS) measurements (Waite et al., 2005) for higher altitudes. The
 203

204 CH₄ number density profile below 1050 km is the average of the profiles de-
205 rived here from VIMS measurements (see section 4). We have extended that
206 profile for altitudes above using the INMS measurements scaled to match our
207 results in the uppermost altitude (1050 km).

208 The population of the V^{7.6} levels (ν_2 and ν_4) is completely dominated by V-T
209 processes (mainly through quenching by N₂, process 1a) from the surface up
210 to about 400 km, where they start to deviate from LTE. Above that altitude,
211 V-T collisions start to be less frequent as the total density decreases and the
212 ν_4 level population is also controlled by absorption of radiation emitted from
213 the warmer layers below. The coupling between ν_2 and ν_4 occurs through the
214 fast collisions with N₂ (process 3a), which affects mainly the population of
215 the more energetic ν_2 level. This level is strongly coupled to ν_4 up to 800 km.
216 Even if the ν_4 -quanta V-V exchange (process 4), which always involves ν_4 , is
217 important for populating and depopulating higher energy levels, it does not
218 affect the population of ν_4 because that is relatively high.

219 At altitudes below 200 km the quenching by N₂ through process 1a is respon-
220 sible for keeping the populations of the V^{3.3} levels ($2\nu_4$, $\nu_2+\nu_4$, ν_1 , ν_3 and
221 $2\nu_2$) close to or in LTE. Above that altitude and up to 700 km, the exchange
222 of ν_4 -quanta (process 4) is however more important and completely couples
223 these levels with ν_4 , which is in LTE, up to 400 km. The absorption of solar
224 radiation is also an important mechanism affecting the population of ν_3 above
225 500 km and $\nu_2+\nu_4$ above 600 km, and, indirectly and only up to 800 km, the
226 rest of the levels in its group ($2\nu_4$, ν_1 and $2\nu_2$) through the strong coupling
227 due to process 3a. The collisions with N₂ through the latter process efficiently
228 redistribute the energy among the levels within the same group, populating
229 the lower energy levels and depopulating the higher energy ones.

230 The effect of the collisional processes on the levels in the $V^{2,3}$ and $V^{1,7}$ groups
231 are analogous to those in $V^{3,3}$. Coupling with the ν_4 level (process 4) is efficient
232 below 500–600 km. Nevertheless, levels in these two groups are out of LTE at
233 all altitudes because, due to their low population, their collisions involving ν_4 -
234 quanta exchange (process 4) and with N_2 through process 1a are not frequent
235 enough. Levels inside each of these groups are strongly coupled among each
236 other up to 500 km due to process 3a. The absorption of solar radiation by
237 the levels in these groups is important at all altitudes.

238 Figure 4 shows the vibrational temperature of the ν_3 level for solar zenith
239 angles (SZA) from 40° to nighttime conditions. As the SZA increases, the
240 population of this level decreases. This behavior occurs because the sunlight
241 travels a longer optical path for a larger SZA and, therefore, suffers a larger
242 absorption. The abrupt changes for SZAs larger than 120° are due to the lack
243 of illumination once the sun sets at those altitudes.

244 3.2 Titan's $3.3 \mu\text{m}$ non-LTE radiance

245 We have used the KOPRA radiative transfer code (Stiller et al., 2002) to
246 simulate CH_4 spectral radiance in the $3.3 \mu\text{m}$ region. We have included the
247 contribution of all bands in Table 3 and used the level populations calculated
248 for the YH-atmosphere described above (see Fig. 3).

249 Figure 5 shows the simulations of the Titan's atmosphere limb CH_4 spectra
250 around $3.3 \mu\text{m}$ at VIMS spectral resolution ($\sim 16 \text{ nm}$) for different tangent alti-
251 tudes and a solar zenith angle of 60° . The contributions from the most impor-
252 tant CH_4 bands are also shown. The emission is centered at 3315 nm and the

253 P-branch (3350–3450 nm) is more intense than the R-branch (3200–3300 nm),
254 mainly due to the asymmetry of the fundamental band ($\nu_3 \rightarrow \text{ground}$). The
255 width of the spectral region where each of the methane contributing bands
256 emit is similar and their Q-branches (3300–3350 nm) peak at similar wave-
257 lengths (always between 3310 and 3360 nm).

258 Figure 6 shows the corresponding integrated radiance for the whole spectral
259 interval (3210 nm–3450 nm) as a function of tangent altitude. The ν_3 funda-
260 mental band dominates the total CH_4 emission above about 750 km. At that
261 altitude, this band is optically thick and the relative contribution to the total
262 emission of the weaker $\nu_3 + \nu_4 \rightarrow \nu_4$ first hot band becomes more important,
263 being the main contribution below. The emission from the $\nu_3 + \nu_2 \rightarrow \nu_2$ first hot
264 band, the $2\nu_3 \rightarrow \nu_3$ second hot band and the ν_3 fundamental band of the minor
265 isotope $^{13}\text{CH}_4$ are about one order of magnitude smaller than the other two
266 at all altitudes, each contributing 5–8% to the total radiance at 650 km. The
267 $\nu_3 + 2\nu_4 \rightarrow 2\nu_4$ and the $\nu_2 + \nu_3 + \nu_4 \rightarrow \nu_2 + \nu_4$ second hot bands contribute about
268 5% each at 500 km. The contribution from other CH_4 bands is negligible.

269 Figure 7 shows the variation of the total CH_4 limb radiance profiles with the
270 SZA. The maximum of the radiance occurs at altitudes around 500 km at
271 all SZAs larger than 90° . This radiance maximum diminishes as the SZA in-
272 creases, according to the behavior of the CH_4 vibrational temperatures (see
273 Fig. 4). Nevertheless, the change of the radiances with SZA is not very acute
274 at almost any altitude until around $\text{SZA} = 90^\circ$. At SZAs larger than 90° , the ra-
275 diance drastically decreases and, although the atmospheric layers above about
276 200 km are illuminated until SZA as large as 110° , the solar radiation does
277 not strongly penetrate at these SZAs.

280 3.3.1 Effect of the collisional rates

281 The population of the vibrational levels at altitudes where collisions are im-
282 portant depend on the rates of the collisional processes involved. In this sec-
283 tion, we investigate the effect of the uncertainty in the collisional rates on the
284 vibrational temperatures for the YH atmosphere and for a SZA=60°.

285 Processes 1a, 1b, 2a and 2b thermalize the vibrational levels and keep ν_2 and
286 ν_4 in LTE below 400 km. Since the N_2 abundance is about 50 times larger
287 than the CH_4 abundance, the quenching with the former is stronger. When
288 increasing the Siddles et al. (1994) collisional rate for N_2 (k_{VT,N_2}) in 50%
289 (they reported measurements errors of 20–25%), the ν_3 vibrational tempera-
290 ture barely changes (not shown).

291 Processes 3a and 3b redistribute the vibrational energy among the levels in
292 a given group through collisions with N_2 and CH_4 , respectively. The more
293 abundant N_2 is significantly more efficient than CH_4 in that redistribution. The
294 rate of this process is reported in Doyennette et al. (1998) and Ménard-Bourcin
295 et al. (2001), who measured a value of $1.8 \times 10^{-11} \text{ cm}^3 \text{ s}^{-1}$ and $6 \times 10^{-11} \text{ cm}^3 \text{ s}^{-1}$,
296 respectively, for the levels in the $V^{1.7}$ group. We used as the nominal rate the
297 mean of both results and scaled it for the other groups of levels ($V^{7.6}$, $V^{3.3}$
298 and $V^{2.3}$) according to the harmonic oscillator law. Decreasing this rate tends
299 to decouple each level to the other levels in its group.

300 The effect on the vibrational temperatures of using the smaller Doyennette

301 et al. (1998)'s rate (Fig. 8) is noticeable below about 1000 km. The ν_3 , $\nu_2+\nu_3$
302 and $2\nu_3$ populations increase at all altitudes where the effect of this process is
303 noticeable, with maximum vibrational temperature variations of 7 K at 650–
304 700 km, 6 K at 550 km, and 9 K at 550 km, respectively. The populations of
305 these levels, with high energy in their groups and highly populated due to
306 absorption of solar radiation, particularly above 700 km, increase because of
307 the reduced de-excitation to lower energy levels when decreasing k_{g,N_2} . Oppo-
308 site to that behavior, those of $2\nu_4$, $3\nu_4$ and $4\nu_4$, with lowest energies of their
309 groups, decrease at all altitudes affected (not shown) because of the reduced
310 de-excitation from higher energy levels. The populations of levels with inter-
311 mediate energy in each group, like $\nu_3+\nu_4$ (in $V^{2.7}$) and $\nu_2+\nu_3+\nu_4$ or $\nu_3+2\nu_4$
312 (in $V^{1.7}$) is also intermediate. Their vibrational temperatures show maximum
313 decrease of 0.5 K at 1000 km, 3 K at 750 km and 5 K at 800 km, and maxi-
314 mum increase of 6 K at 550 km, 3 K at 500 km and 7 K at 500 km, respectively.
315 These levels are mainly coupled to higher energy levels highly populated by
316 solar absorption in their groups, like $\nu_2+\nu_3$ and $2\nu_3$ respectively, above 600–
317 800 km, and to the least energetic levels, like $3\nu_4$ and $4\nu_4$ respectively, below.
318 Therefore, the decrease in this rate reduces the number of molecules relaxing
319 to those levels from higher energy levels above those altitudes, decreasing their
320 populations, and from these levels to the lower energy levels below, increasing
321 their populations.

322 The response of the vibrational temperatures when using the larger rate of
323 Ménard-Bourcin et al. (2001) is the opposite, but slightly smaller (not shown),
324 which is an example of the non-linear response of the vibrational levels popula-
325 tions to changes in the processes rates. Process 3b barely affects the population
326 of the CH_4 levels.

327 The impact of the change of the rate of process 3a (k_{g,N_2}) on the simulated CH_4
328 $3.3\ \mu\text{m}$ (3200–3500 nm) integrated limb radiance is shown in Fig. 9 (red and
329 green lines), which mainly reflects the change in the vibrational temperatures
330 of the ν_3 and the $\nu_3+\nu_4$ levels, the main responsables of the methane total
331 radiance (see Fig. 6). It is noticeable ($>5\%$) at altitudes below 850 km, where
332 the ν_3 level vibrational temperature starts to be affected by the uncertainty
333 in this process (see Fig. 8) and increases as the tangent height decreases. The
334 radiance change is smaller than 10% above 750 km and smaller than 25% above
335 650 km. It is maximum around 500 km (45% more radiance when using the
336 smaller rate of Doyennette et al. (1998) and 20% less radiance when using the
337 larger rate of Ménard-Bourcin et al. (2001)), where the maximum contribution
338 of the first hot band ($\nu_3+\nu_4\rightarrow\nu_3$) to the total radiance occurs.

339 Process 4, representing ν_4 -quanta exchange with the ν_4 level, connects levels of
340 different groups containing ν_4 -quanta ($\nu_4\neq 0$) and, in fact, is the most impor-
341 tant process coupling different groups of levels. Decreasing its rate k_{vv4} reduces
342 the vibrational energy transfer from the higher energy ν_4 -quanta levels to ν_4 ,
343 leading to larger populations of the former. Ultimately, that also affects the
344 population of the other levels in their groups through process 3a. For example,
345 a k_{vv4} decrease translates into larger populations of not only the $2\nu_4$ level,
346 driven by the slowest V-V exchange with the ν_4 , but also of the other levels
347 in $V^{3.3}$, driven by the lower $2\nu_4$ population. This behavior is similar for the
348 other groups of levels, except for the $V^{7.6}$ group, which population decreases
349 (although not dramatically since the population of ν_4 is more than two orders
350 of magnitude larger than other ν_4 -quanta levels).

351 Avramides and Hunter (1983) reported a k_{vv4} value of $4.1\times 10^{-11}\ \text{cm}^3\text{s}^{-1}$.
352 Doyennette et al. (1998), Hess et al. (1980), and Ménard-Bourcin et al. (2001)

353 also measured this rate and provided values of $9.2 \times 10^{-11} \text{ cm}^3 \text{ s}^{-1}$, $1.8 \times 10^{-11} \text{ cm}^3 \text{ s}^{-1}$,
354 and $1.2 \times 10^{-11} \text{ cm}^3 \text{ s}^{-1}$, respectively. More recently, Boursier et al. (2007) re-
355 ported rates of 2.2, 3.3 and $4.4 \times 10^{-11} \text{ cm}^3 \text{ s}^{-1}$ for the ν_4 -quanta exchange in-
356 volving $2\nu_4$, $3\nu_4$ and $4\nu_4$, respectively. We selected a nominal rate of $4.1 \times 10^{-11} \text{ cm}^3 \text{ s}^{-1}$
357 because, using the CH_4 mixing ratio measured by GCMS (Niemann et al.,
358 2005), that provided the best fit to VIMS limb radiance at 500–600 km. In
359 that altitude range, methane is still well mixed (Yelle et al., 1997; Lara et al.,
360 1996) and the contribution to the signal due to aerosol scattering is not sig-
361 nificant, since the measurements are above Titan’s haze layer (Adriani et al.,
362 2011; Porco et al., 2005).

363 The effect of using the slowest value for $k_{\nu\nu_4}$ (Doyennette et al., 1998) is shown
364 in Fig.10. Since absorption of solar radiation and process 3a dominate the level
365 populations above 700 km, the effect of this rate is only noticeable below that
366 altitude. Maximum changes in the vibrational temperatures are 5 K at 500 km,
367 4–5 K at 400 km and 2–10 K at 300 km for the the main $3.3 \mu\text{m}$ emitting levels
368 in the $V^{3.3}$, $V^{2.3}$ and $V^{1.7}$ groups, respectively. The magnitude of the effect
369 on a level within each of these three groups depends on its coupling with the
370 $2\nu_4$, $3\nu_4$ and $4\nu_4$, as the case may be, which are the ones suffering the largest
371 decreases in their populations. For example, the change of the $\nu_3+2\nu_4$ T_v is
372 larger than that of the $\nu_2+\nu_3+\nu_4$ because the former is more strongly coupled
373 to $4\nu_4$ through process 3a, due to their closer energy. The smallest Doyennette
374 et al. (1998) rate is still large enough to keep $2\nu_4$ completely coupled to ν_4
375 below 350 km, in LTE. Since the levels in the $V^{3.3}$ group are also completely
376 coupled to $2\nu_4$ at those altitudes, their populations remain unchanged there
377 (see ν_3 in Fig.10).

378 The corresponding change in the limb radiance is shown in Fig.9 (dark blue

379 line) and occurs at altitudes below 600 km, increasing by 20% around 400 km.

380 That variation mainly reflects the change in the $\nu_3+\nu_4$ level population because
381 the contribution from the first hot band is significantly larger than from the
382 fundamental band at the tangent heights where the variation in $k_{\nu\nu 4}$ affects
383 the ν_3 population (400–600 km).

384 Current uncertainties in processes 5 and 6 produce changes in vibrational
385 temperature smaller than 0.5 K (not shown).

386 3.3.2 *Effect of p-T profile*

387 We compared the vibrational temperatures and the number densities of the
388 CH₄ levels for two distinct pressure-temperature (p-T) profiles: a) the com-
389 bined Yelle-HASI profile described in the previous sections (YH-atmosphere);
390 and b) the atmosphere recommended in Yelle’s engineering model (Yelle et al.,
391 1997) (hereafter Y-atmosphere). In order to isolate the effect of the p-T pro-
392 file, we kept, for this test, the same CH₄ number density for both reference
393 atmospheres. The differences between the total number densities in these two
394 cases are shown in Fig. 11. The Y-Atmosphere is 20% less dense below 500 km,
395 50% less dense at 650 km and 70% less dense above 800 km.

396 Figure 12 shows the kinetic temperatures (black lines) and the corresponding
397 vibrational temperatures of the main 3.3 μm emitting CH₄ vibrational levels
398 calculated for these two reference atmospheres. The populations of the CH₄
399 levels remain essentially unchanged above 1000 km for both atmospheres be-
400 cause they are driven exclusively by absorption of solar radiation at those
401 altitudes. The smaller density of the Y-atmosphere implies a smaller N₂ abun-
402 dance, which makes collisions through process 3a less frequent and, thus, the

403 energy re-distribution among the levels in the groups less efficient. Therefore,
404 the effect above 600 km behaves as a decrease in the k_{gN_2} rate. Below that
405 altitude, process 4 is also important and there is an additional effect driven
406 by the ν_4 population. Since the ν_4 level is very close to LTE at those alti-
407 tudes, the change in kinetic temperature is translated into a similar change
408 in the vibrational temperature of the ν_4 level. The rest of the levels are also
409 affected through their coupling with the ν_4 level (process 4) at those altitudes,
410 particularly, the $V^{3.3}$ levels.

411 The lighter Y-atmosphere increases the ν_3 vibrational temperature 5 K around
412 750 km. That is also the response of levels $\nu_3+\nu_4$ and $\nu_2+\nu_3$, although the
413 change is smaller (2 K). In the same way, the $2\nu_3$ population is 6 K larger for
414 the Y-atmosphere whereas those of the lower energy levels of the $V^{1.7}$ group
415 ($\nu_3+2\nu_4$ and $\nu_2+\nu_3+\nu_4$) are smaller (2 and 7 K, respectively). The response
416 of the populations is smaller or even the opposite at altitudes below 600 km
417 because it is compensated through the effect of process 4, which directly or
418 indirectly links all levels to ν_4 . The population of the latter at those altitudes
419 is close to LTE and affected by changes in the local kinetic temperature and,
420 therefore, is smaller for the colder Y-atmosphere. That lowers the population
421 of the rest of the levels. The effect of the Y-atmosphere on the emitter levels
422 vibrational temperatures is smaller than 1 K below 600 km, except for ν_3 below
423 450 km, which is completely coupled to ν_4 at those altitudes (and thus in LTE)
424 and suffers a maximum decrease of 10 K around 200 km.

425 These changes in the vibrational temperatures produce a change in the inte-
426 grated radiance smaller than 10% above 800 km and below 600 km and smaller
427 than 20% at the remaining altitudes (see Fig. 9). This is an important result
428 because the radiance at a given tangent altitude depends on the pressure and

429 temperature structure below that altitude. Note that this effect is different
430 from that directly induced by the pressure and temperature on the number
431 density of the ground state (and hence on the upper state). The former acts
432 through the effectiveness of the excitation process, while the second is induced
433 by the number density of the ground state of the transition.

434 3.3.3 Effect of the CH_4 abundance

435 We have also isolated the effect of the CH_4 abundance for a fixed p-T pro-
436 file. This test demonstrates the need of an iterative methane retrieval scheme
437 in which an update of the vibrational temperatures in each iteration is nec-
438 essary. We used the YH-atmosphere with two different CH_4 volume mixing
439 ratio (vmr) profiles: the one derived here extended with Cassini-INMS mea-
440 surements above 1050 km and the one from the recommended model by Yelle
441 et al. (1997) merged to a constant vmr below 650 km (see Fig. 17). The differ-
442 ence between these two vmr profiles is 100–200% from 800 to 1200 km (being
443 the one derived here smaller), and it decreases below to be almost the same
444 at 700 km. The vibrational temperatures calculated for these cases are shown
445 in Fig. 13.

446 The vibrational temperatures barely change except that of the ν_3 level, which
447 is 5 K smaller around 800 km for the larger Yelle CH_4 abundance. That smaller
448 excitation is due to less solar radiation reaching that altitude, reduced at
449 altitudes above by a larger absorption caused by the larger abundance of CH_4
450 molecules. Below 1100 km, the fundamental band ($\nu_3 \rightarrow \text{ground}$) stops being
451 optically thin and a smaller solar flux reaches the altitudes below (that is why
452 the vibrational temperature of the ν_3 level starts to decrease at that altitude).

453 In consequence, the absorption of solar radiation decreases at 800 km when
454 increasing the CH_4 abundance above. For the other bands, the sensitivity to
455 a CH_4 density change is less pronounced because they become optically thick
456 at lower altitudes, where collisions are more important.

457 Figure 9 shows the corresponding effect on the $3.3\ \mu\text{m}$ integrated radiance.
458 When increasing the CH_4 volume mixing ratio, the number density for most
459 levels show similar changes to that of the ground level. That of ν_3 increases to
460 a lesser extent due the smaller vibrational temperature. Taking into account
461 the non-linear behavior of the limb radiance, the overall increase produced by
462 the Yelle et al. (1997) CH_4 volume mixing ratio is 15% at 700 km and 40% at
463 950 km, i.e., smaller than the corresponding change in the CH_4 abundance.

464 **4 Analysis of the Measurements and Retrieval of CH_4 abundance**

465 We have analyzed VIMS daytime observations measured during two Titan's
466 flybys, containing 4 different cubes (see Table 1). Our data selection criteria
467 left measurements taken only in the southern hemisphere. Figure 14 shows
468 mean the VIMS measured spectrum in the $3.3\ \mu\text{m}$ region during daytime
469 (solid line) at a tangent height of 650 km. The spectrum has been averaged
470 from 20 individual spectra covering solar zenith angles from 42° to 70° and
471 interpolated in tangent height. The simulated non-LTE methane spectrum
472 (dashed black line) is also shown, calculated at a tangent height of 650 km
473 and for $\text{SZA}=60^\circ$, using the CH_4 abundance retrieved in this work (see be-
474 low). The shape of the complete CH_4 $3.3\ \mu\text{m}$ band (3200–3450 nm) measured
475 by VIMS agrees very well with our simulations at that tangent height. The
476 radiance in the spectral region of 3300–3450 nm (Q- and P-branches) is well

477 reproduced at all altitudes. However, the radiance in the 3200–3300 nm region
478 (R-branch) increases relative to the other branches at altitudes above about
479 750 km (not shown). The magnitude of that excess of emission is similar to the
480 CH₄ emission in the R-branch for all daytime spectra analyzed. That excess
481 of emission does not originate from CH₄ because all main emitting bands have
482 been included in our calculations and, additionally, no CH₄ band emission can
483 be equally or more intense than that from the main isotope fundamental band
484 at those altitudes. Furthermore, no known CH₄ band shows its maximum in-
485 tensity between 3250 and 3300 nm nor shows such a large asymmetry between
486 its P- and R-branches. Further analysis of that emission is beyond the scope
487 of this paper. The accurate modeling of the CH₄ component presented here
488 can be then used to isolate and characterize that interfering emission. Thus,
489 in order to avoid systematic errors in our retrievals due to emission not arising
490 from CH₄, we only used the spectral region covering the Q- and P-branches
491 (3299.5 to 3497.9 nm) at all altitudes.

492 Figure 15 shows the radiance integrated in the spectral interval used in our
493 retrievals (3299.5–3497.9 nm), approximately the regions of the Q- and P-
494 branches, averaged over the 20 cases studied at tangent heights from 500 to
495 1500 km. The figure also shows the noise of a single measurement, which is
496 similar to the signal around 1100 km. Hence, we retrieved methane from VIMS
497 spectra only up to 1050 km.

498 Titan's limb atmospheric emission has been simulated in the retrieval with the
499 Geofit Broad Band (GGB) radiative transfer code, originally designed for the
500 Earth atmosphere. This code is the self standing version of the forward model
501 internal to the Geo-fit Multi-Target Retrieval (GMTR) system (Carlotti et al.,
502 2006) updated to perform simulations over a broad frequency interval using

503 a line by line cross sections computation. The GBB code has been upgraded
 504 introducing VIMS instrumental characteristics (field of view and spectral in-
 505 strumental response) along with the possibility to compute the limb radiance
 506 in non-LTE. The latter was taken into account using the non-LTE population
 507 ratios previously calculated by GRANADA and Eqs. 10 and 14 of Edwards
 508 et al. (1993), that account for the non-LTE absorption coefficients and source
 509 function, respectively. The computed radiances have been validated with the
 510 non-LTE computations made with the KOPRA radiative transfer algorithm
 511 (Stiller et al., 2002) used in previous sections.

512 The modified GBB forward model has been included in a retrieval code that
 513 exploits the optimal estimation technique (Rodgers, 2000) and the global fit
 514 technique (Carlotti et al., 2006) to retrieve the volume mixing ratios (vmr) of
 515 Titan’s atmospheric gases from VIMS limb radiance. The non-LTE popula-
 516 tions of the CH₄ vibrational levels were computed with the non-LTE model
 517 described above. The retrieval procedure minimizes the cost function through
 518 the Gauss Newton iterative procedure. At each iteration the solution is ex-
 519 pressed by

$$520 \quad x_{i+1} = x_i + (K^T S_m^{-1} K + S_a^{-1})^{-1} (K^T S_m^{-1} \bar{n} - S_a^{-1} (x_i - x_a)) \quad (2)$$

521 where x_i is the vector of the solution at iteration i , K is the jacobian matrix
 522 containing the derivatives of the observations with respect to the retrieved
 523 parameters, S_m is the variance covariance matrix (VCM) of the measurements,
 524 x_a and S_a are, respectively, the a-priori values of the parameters and their
 525 VCM, and \bar{n} is the vector containing the differences between the observed and
 526 the simulated radiances.

527 In our retrieval code, the derivatives of the spectra with respect to the retrieved
528 parameters (the jacobians, K) have been computed numerically. The spectra
529 have been simulated on a frequency grid of 0.0005 cm^{-1} , in order to properly
530 model the shape of the lines at the low pressures typical of Titan mesosphere,
531 and then convolved with the VIMS spectral response function. All $3.3 \mu\text{m}$ CH_4
532 bands indicated in Table 3 (including those of the $^{13}\text{CH}_4$ isotopologue) have
533 been included in the line by line computation. To avoid underestimation of
534 the computed radiances, a very low threshold for the line strength of the lines
535 included in the computation has been used ($0.10 \times 10^{-32} \text{ cm}^{-1} \text{ molecule}^{-1} \text{ cm}^2$
536 at 296 K).

537 The CH_4 abundance retrieval scheme used consisted in two main loops. In
538 the inner loop, the CH_4 vibrational temperatures were kept constant and the
539 volume mixing ratio was derived using the method described above. After
540 convergence, the vibrational temperatures were updated in the outer loop
541 using the non-LTE model and the vmr retrieved in the previous iteration.
542 The a priori CH_4 vmr profile used was that derived from GCMS measurements
543 (Niemann et al., 2005) below 500 km and Cassini-INMS measurements (Waite
544 et al., 2005) above, and the a-priori errors were set to 100% of the a-priori
545 profile.

546 We have retrieved a single vmr profile from each single spectra profile, with
547 SZA limited to 70° to avoid inhomogeneties of non-LTE. In total 20 obser-
548 vations coming from 4 different VIMS cubes have been analysed (see Table
549 1). The retrieved individual CH_4 volume mixing ratio profiles are shown in
550 Fig. 16. Typical noise retrieval errors for the individual profiles range from
551 1000 to 2000 ppmv (10–15%). The systematic errors in the retrieved pro-
552 files come mainly from the uncertainty in the non-LTE parameters (mainly

553 k_{g,N_2}) and from uncertainties in the assumed pressure-temperature. From the
554 analysis in section 3.3, overall they are estimated to be 7% at 1050 km, 25%
555 at 850 km and 60% at 650 km. These are significantly larger than systematic
556 instrumental errors.

557 Figure 16 also shows the mean retrieved CH_4 profile, with a standard deviation
558 ranging from 1200 ppmv at 650 km to 7000 ppmv at 1050 km. Except for two
559 outlier profiles, the retrieved methane profiles are rather compacted, which
560 suggests a weak dependence of the methane abundance on latitude. Our mean
561 profile also suggests that the CH_4 abundance does not strongly deviate (less
562 than 30% up to 850 km and less than 60% up to 1050 km) from its well mixed
563 value of 1.4×10^4 ppmv around 600 km.

564 We have compared our results with those from models and other measure-
565 ments. Figure 17 shows comparisons between the average CH_4 volume mixing
566 ratio profile derived here with those from the Yelle et al. (1997) recommended
567 and maximum engineering models, the Wilson and Atreya (2004), the updated
568 Lara et al. (1996) (with updated chemistry and eddy diffusion coefficient as
569 described in Pernot et al. (in preparation)), the Krasnopolsky (2009), and the
570 Müller-Wodarg et al. (2008) models.

571 The CH_4 vmr derived in this work is about 50% smaller than the calculations
572 from the Yelle (1997) recommended model, which were obtained using inter-
573 mediate total mass densities and provided intermediate CH_4 vmr. It agrees
574 within 25% with calculations from his maximum model, which were obtained
575 using maximum total mass densities and provided minimum CH_4 vmr. We
576 note that if we used in our retrievals the smaller densities of the Yelle's rec-
577 ommended model, we would retrieve an almost proportionally larger CH_4 vmr

578 (which would lead to a better agreement with Yelle's recommended CH_4 vmr)
579 but a very similar CH_4 number density (see section 3.3.2), and, hence, the com-
580 parison with Yelle's recommended CH_4 number density would not improve (see
581 below).

582 Our CH_4 vmr is about 25% smaller than the results from Wilson and Atreya
583 (2004) below 950 km. The Lara et al. (1996) CH_4 vmr profile agrees very well
584 with our measurements below 900 km (within 10%) and shows slightly lower
585 values (20%) above. Our derived CH_4 vmr is in very good agreement with that
586 from the Krasnopolsky (2009) model (within 10%) at all altitudes, except for
587 the upper limit of our retrievals (1050 km), where our value is 35% smaller.
588 Nevertheless, Müller-Wodarg et al. (2008) provide smaller values at that upper
589 limit and show a good agreement with our retrieved methane vmr. Hence,
590 VIMS measurements support those models which show a weak deviation from
591 well mixed values from the lower atmosphere up to 1000 km.

592 In order to reduce the errors originated by the assumed p-T profile, we have
593 also compared the CH_4 number density profiles, calculated using the retrieved
594 volume mixing ratio and the p-T profile described in Section 3.1. Note that
595 the errors due to the p-T profile are not completely avoided since they also
596 propagate through the modeling of the levels non-LTE populations. The com-
597 parisons are shown in Fig. 18. The methane number density retrieved in this
598 work is within the range of the values in Yelle et al. (1997) (between their
599 recommended and their minimum models below 700 km and between the rec-
600 ommended and their maximum models above). Our methane number density
601 measurements agree very well with the calculations from the updated Lara
602 et al. (1996) model up to 700 km. It is larger (up to 50%) at altitudes above.
603 The measurements from Voyager reported in Vervack et al. (2004) are also

605 Imaging Spectrometer (UVIS) Shemansky et al. (2005) show up to 50% larger

606 values below 650 km and up to 50% smaller above.

607 **5 Summary and Conclusions**

608 We have analyzed Cassini-VIMS $3.3\ \mu\text{m}$ limb radiance measured in Titan's
609 upper atmosphere (450–1100 km). These emissions mainly originate from the
610 strong methane ν_3 band and, due to the low atmospheric density at those
611 altitudes, they are far from local thermodynamic equilibrium (LTE). We have
612 developed a sophisticated non-LTE model for methane in Titan after the adap-
613 tation of the Generic RAdiative traNsfer AnD non-LTE population Algorithm
614 (GRANADA) code for the Earth described in Funke et al. (2007). Our model
615 calculates the non-LTE populations of 18 CH_4 vibrational levels of the main
616 CH_4 isotope and 4 of the $^{13}\text{CH}_4$ minor isotope. Our main findings regarding
617 the behavior of the non-LTE populations during daytime are:

- 618 • Absorption of solar radiation is the only excitation mechanism controlling
619 the population of levels containing ν_3 -quanta above 1000 km.
- 620 • Collisions between methane and molecular nitrogen which redistribute the
621 vibrational energy among the levels in each vibrational level group is the
622 most important collisional process determining the populations of the levels
623 with ν_3 -quanta. This process affects their populations at altitudes below
624 1000 km.
- 625 • Vibrational-thermal (V-T) collisions relaxing excited molecules to lower en-
626 ergy groups do not play a major role on the populations of the CH_4 levels,
627 except for ν_4 and ν_2 , for which they are important and keep them very close

- 629 • Vibrational energy exchange of ν_4 -quanta is important below 500 km and
 630 couples the high energy levels with the ν_4 state. Levels in group $V^{3.3}$ ($2\nu_4$,
 631 $\nu_2+\nu_4$, ν_1 , ν_3 and $2\nu_2$) are in LTE below 400 km due to this process. Based on
 632 our simulations of Titan's 3.3 μm emission, we suggest a value of $4.1 \text{ cm}^3\text{s}^{-1}$
 633 for the rate of these collisions.
- 634 • Uncertainties in the collisional rates (mainly in the redistribution of vibra-
 635 tional energy in N_2 collisions, and also in vibrational energy exchange of
 636 ν_4 -quanta below 600 km) yield vibrational temperature errors of up to 8 K,
 637 5 K and 9 K of ν_3 , $\nu_3+\nu_4$ and $2\nu_3$, respectively. The pressure-temperature
 638 structure affects the vibrational temperatures through the nitrogen num-
 639 ber density above 600 km and through the temperature profile below. The
 640 vibrational temperatures increase 5 K for ν_3 and $2\nu_3$ and 2 K for $\nu_3+\nu_4$ at
 641 700 km due to the change from the pressure-temperature profiles assumed
 642 in this work to that of Yelle et al. (1997).

643 Using the non-LTE model, we have simulated 3.3 μm Titan's limb radiance at
 644 VIMS spectral resolution from 350 to 1100 km and found that:

- 645 • The daytime radiance maximum occurs around 500 km and moves slightly
 646 upwards with increasing solar zenith angle, peaking at 700 km at $\text{SZA}=100^\circ$.
- 647 • The main contributor to the total limb radiance is the CH_4 ν_3 fundamental
 648 band ($\nu_3 \rightarrow \text{ground}$) above 750 km and the $\nu_3+\nu_4 \rightarrow \nu_4$ first hot band below.
 649 The contribution from the $\nu_3+\nu_2 \rightarrow \nu_2$ first hot band range from 5 to 8% at
 650 altitudes below 800 km. Emission from the $^{13}\text{CH}_4$ isotope fundamental band
 651 is 7% of the total around 600–700 km and about 5% below. Contribution
 652 from the $2\nu_3 \rightarrow \nu_3$ band is about 5% below 750 km. Contribution from other
 653 weaker bands ($\nu_2+\nu_3+\nu_4 \rightarrow \nu_2+\nu_4$ and $\nu_3+2\nu_4 \rightarrow 2\nu_4$) add from 5% at 650 km

654 to almost 10% of the total radiance at 400 km. The latter strengthens the
655 importance of modeling those bands for an accurate analysis of methane
656 3.3 μm radiance.

657 • Errors in the simulated radiance arising from uncertainties in the collisional
658 rates are 5% above 900 km, 25% at 600 km and 50% at 400 km. The radiance
659 sensitivity study to the pressure-temperature shows changes from the profile
660 assumed here to that from Yelle et al. (1997) of 4% above 900 km, 17% at
661 650 km, and 10% below.

662 We have compared our radiance simulations with measurements of Titan's
663 3.3 μm Cassini-VIMS limb daytime emission and found that methane spectra
664 alone is not able to explain the shape of the VIMS 3.3 μm spectra. An emission
665 not originating from CH_4 overlaps the CH_4 v_3 R-branch. This emission is
666 present in all daytime spectra analyzed above 800 km. The spectral position,
667 tangent altitudes and magnitude of the emission allow us to assure that it is
668 not due to missing CH_4 bands in our simulations. Further analysis on that
669 emission will be subject of a future work.

670 We have retrieved methane abundance in the southern hemisphere from Cassini-
671 VIMS 3.3 μm measurements on the P- and Q-branches considering non-LTE.
672 Our results show no significant latitudinal methane variation. The average
673 retrieved methane volume mixing ratio does not vary strongly with altitude.
674 Below 850 km, it deviates less than 30% from the value at the lower limit
675 of our retrieval and shows a slightly larger gradient above, reaching 2.5×10^4
676 ppmv around 1000 km. Typical noise errors of the retrieved profiles are 10–15%
677 whereas systematic errors (coming mainly from uncertainties in the collisional
678 rates and pressure-temperature) are 7%, 25% and 60% at at 1050, 850 and
679 650 km, respectively. Comparisons with measurements from other instruments

680 show that our retrieved VIMS CH₄ number densities are 10 to 50% smaller
681 than the Shemansky et al. (2005) Cassini-UVIS measurements below 650 km
682 and 10 to 50% larger than results from Voyager (Vervack et al., 2004) and from
683 Cassini-UVIS (Shemansky et al., 2005) above. Our derived methane volume
684 mixing ratio is within the limits of the Yelle et al. (1997) model and in excel-
685 lent agreement with the Krasnopolsky (2009), the updated Lara et al. (1996)
686 and the Müller-Wodarg et al. (2008) models. It is smaller than calculations
687 from Wilson and Atreya (2004) at all altitudes. VIMS measurements support
688 those models which show a weak deviation from well mixed values from the
689 lower atmosphere up to 1000 km.

690 **Acknowledgements**

691 The IAA team was supported by the Spanish MICINN, under project AYA2008-
692 03498/ESP, and EC FEDER funds. They also thank the Spanish MICINN for
693 funding support through the CONSOLIDER program ASTROMOL CSD2009-
694 00038. The authors would like to thank the team of the University of Bour-
695 gogne, in particular Vincent Boudon, for providing CH₄ spectral data, and
696 Luisa M. Lara for providing the updated methane calculations from the Lara
697 et al. (1996) model.

698 **References**

- 699 Acton, C. H., 1996. Ancillary data services of NASA's Navigation and Ancil-
700 lary Information Facility. *Planetary and Space Science* 44, 65–70.
- 701 Adriani, A., Dinelli, B. M., Lopez-Puertas, M., Garcia-Comas, M., Moriconi,

702 M. L., Funke, B., 2011. Vertical profiles of HCN in Titan's atmosphere
703 from non-LTE emission at 3 microns by Cassini/VIMS observations. *Icarus*
704 submitted.

705 Appleby, J. F., 1990. CH₄ nonlocal thermodynamic equilibrium in the at-
706 mospheres of the giant planets. *Icarus* 85, 355–379.

707 Avramides, E., Hunter, T. F., 1983. Vibrational-vibrational and vibrational-
708 translational/rotational processes in methane, oxygen gas-phase mixtures.
709 *Mol. Phys.* 48, 1331–1343.

710 Baines, K. H., et al., 2006. On the discovery of co nighttime emissions on
711 titan by cassini/vims: Derived stratospheric abundances and geological im-
712 plications. *Planet. Space Sci.* 54, 1552–1562.

713 Baines, K. H., et al., 2005. The Atmospheres of Saturn and Titan in the
714 Near-Infrared First Results of Cassini/vims. *Earth Moon and Planets* 96,
715 119–147.

716 Boursier, C., Ménard, J., Ménard-Bourcin, F., 2007. Vibrational relaxation of
717 methane by oxygen collisions: Measurements of the near-resonant energy
718 transfer between CH₄ and O₂ at low temperature. *J. Phys. Chem. A* 111,
719 7022–7030.

720 Brown, R., et al., 2006. Observations in the Saturn system during approach
721 and orbital insertion, with Cassini's Visual and Infrared Mapping Spectrom-
722 eter (VIMS). *Astron. Astrophys.* 446, 707–716.

723 Brown, R. H., et al., 2004. The Cassini Visual And Infrared Mapping Spec-
724 trometer (VIMS) investigation. *Space Sci. Rev.* 115, 111–168.

725 Carlotti, M., Brizzi, G., Papandrea, E., Prevedelli, M., Ridolfi, M., Dinelli,
726 B. M., Magnani, L., 2006. GMTR: Two-dimensional geo-fit multitarget re-
727 trieval model for Michelson Interferometer for Passive Atmospheric Sound-

- 729 Clark, R., et al., 2010. Detection and mapping of hydrocarbon deposits on
730 titan. *J. Geophys. Res.* in press.
- 731 Coustenis, A., et al., 2006. Titan’s 3-micron spectral region from ISO high-
732 resolution spectroscopy. *Icarus* 180, 176–185.
- 733 Cruikshank, D. P., et al., 2009. Carbon dioxide on the satellites of Saturn:
734 Results from the Cassini VIMS investigation and revisions to the VIMS
735 wavelength scale. *Icarus* in press, doi:10.1016/j.icarus.2009.07.012.
- 736 Doyennette, L., Menard-Bourcin, F., Menard, J., Boursier, C., Camy-Peyret,
737 C., 1998. Vibrational energy transfer in methane excited to v_3 in CH_4 -
738 N_2/O_2 mixtures from laser-induced fluorescence measurements. *J. Phys.*
739 *Chem.* 102, 3849–3855.
- 740 Edwards, D. P., López-Puertas, M., López-Valverde, M. Á., 1993. Non-local
741 thermodynamic equilibrium studies of the $15\ \mu\text{m}$ bands of CO_2 for at-
742 mospheric remote sensing. *J. Geophys. Res.* 98 (D8), 14,955–14,977.
- 743 Filacchione, G., 2006. Calibrazioni a terra e prestazioni in volo di spettrometri
744 ad immagine nel visibile e nel vicino infrarosso per l’esplorazione planetaria.
745 Ph.D. thesis, INAF-IASF, Rome, Italy.
- 746 Filacchione, G., et al., 2007. Saturn’s icy satellites investigated by Cassini-
747 VIMS. I. Full-disk properties: 350–5100 nm reflectance spectra and phase
748 curves. *Icarus* 186, 259–290.
- 749 Fulchignoni, M., et al., 2005. In situ measurements of the physical character-
750 istics of titan’s environment. *Nature* 438, 785–791.
- 751 Funke, B., et al., 2007. Analysis of nonlocal thermodynamic equilibrium CO
752 $4.7\ \mu\text{m}$ fundamental, isotopic and hot band emissions measured by the
753 Michelson Interferometer for Passive Atmospheric Sounding on Envisat. *J.*

- 755 Funke, B., et al., 2009. Carbon monoxide distributions from the upper tro-
756 posphere to the mesosphere inferred from 4.7 μm non-local thermal equilib-
757 rium emissions measured by MIPAS on Envisat. *Atmos. Chem. Phys.* 9 (7),
758 2387–2411.
- 759 Geballe, T. R., Kim, S. J., Noll, K. S., Griffith, C. A., 2003. High-resolution
760 3 micron spectroscopy of molecules in the mesosphere and troposphere of
761 Titan. *Astrophys. J.* 583, L39–L42.
- 762 Hess, P., Kung, A., Moore, C., 1980. Vibration→vibration energy transfer in
763 methane. *J. Chem. Phys.* 72, 5525–5531.
- 764 Kim, S. J., Geballe, T. R., Noll, K. S., Courtin, R., 2005. Clouds, haze, and
765 CH_4 , CH_3D , HCN , and C_2H_2 in the atmosphere of Titan probed via 3 μm
766 spectroscopy. *Icarus* 173, 522–532.
- 767 Kim, S. J., Geballe, T. R., Noll, K. S., 2000. Note: Three-micrometer CH_4 line
768 emission from Titan’s high-altitude atmosphere. *Icarus* 147, 588–591.
- 769 Krasnopolsky, V. A., 2009. A photochemical model of Titan’s atmosphere and
770 ionosphere. *Icarus* 201, 226–256.
- 771 Lara, L. M., Lellouch, E., López-Moreno, J. J., Rodrigo, R., 1996. Vertical
772 distribution of Titan’s atmospheric neutral constituents. *Journal of Geo-*
773 *physical Research* 101, 23261–23283.
- 774 López-Puertas, M., Taylor, F. W., 2001. Non-LTE radiative transfer in the
775 Atmosphere. World Scientific Pub., Singapore.
- 776 McCord, T. B., et al., 2004. Cassini VIMS observations of the Galilean satel-
777 lites including the VIMS calibration procedure. *Icarus* 172, 104–126.
- 778 Ménard-Bourcin, F., Boursier, C., Doyennette, L., Ménard, J., 2001. Rovibra-
779 tional energy transfer in methane excited to $2\nu_3$ in $\text{CH}_4\text{--N}_2$ mixtures from

- 780 double-resonance measurements. *J. Phys. Chem. A* 105, 11446.
- 781 Müller-Wodarg, I. C. F., Yelle, R. V., Cui, J., Waite, J. H., 2008. Horizontal
782 structures and dynamics of Titan's thermosphere. *Journal of Geophysical*
783 *Research (Planets)* 113 (E12), 10005.
- 784 Negrão, A., et al., 2006. Titan's surface albedo variations over a Titan season
785 from near-infrared CFHT/FTS spectra. *Planet. Space Sci* 54, 1225–1246.
- 786 Niemann, H. B., et al., 2005. The abundances of constituents of Titan's at-
787 mosphere from the GCMS instrument on the Huygens probe. *Nature* 438,
788 779–784.
- 789 Pernot, P., et al., in preparation. Intercomparison of 1D photochemical models
790 of Titan's atmosphere.
- 791 Porco, C. C., et al., 2005. Imaging of Titan from the Cassini spacecraft. *Nature*
792 434, 159–168.
- 793 Rodgers, C. D., 2000. *Inverse Methods for Atmospheric Sounding: Theory and*
794 *Practice*. Vol. 2 of Series on Atmospheric, Oceanic and Planetary Physics,
795 F. W. Taylor, ed. World Scientific.
- 796 Rothman, L. S., et al., 2005. The *HITRAN* 2004 molecular spectroscopic data-
797 base. *J. Quant. Spectrosc. Radiat. Transfer* 96, 139–204.
- 798 Seo, H., Kim, S. J., Kim, J. H., Geballe, T. R., Courtin, R., Brown, L. R.,
799 2009. Titan at 3 microns: Newly identified spectral features and an improved
800 analysis of haze opacity. *Icarus* 199, 449–457.
- 801 Shemansky, D. E., Stewart, A. I. F., West, R. A., Esposito, L. W., Hal-
802 lett, J. T., Liu, X., 2005. The Cassini UVIS Stellar Probe of the Titan
803 Atmosphere. *Science* 308, 978–982.
- 804 Siddles, R., Wilson, G. J., Simpson, C. J. S. M., 1994. The vibrational de-
805 activation of the bending modes of CD₄ and CH₄ measured down to 90 k.

- 807 Stiller, G. P., et al., 2002. Sensitivity of trace gas abundances retrievals from
808 infrared limb emission spectra to simplifying approximations in radiative
809 transfer modelling. *J. Quant. Spectrosc. Radiat. Transfer* 72 (3), 249–280.
- 810 Tobiska, W. K., et al., 2000. The SOLAR2000 empirical solar irradiance model
811 and forecast tool. *J. Atmos. Solar-Terr. Phys.* 62, 1233–1250.
- 812 Vervack, R. J., Sandel, B. R., Strobel, D. F., 2004. New perspectives on titan's
813 upper atmosphere from a reanalysis of the voyager 1 uvs solar occultations.
814 *Icarus* 170, 91–112.
- 815 Waite, J. H., et al., 2005. Ion Neutral Mass Spectrometer Results from the
816 First Flyby of Titan. *Science* 308, 982–986.
- 817 Wenger, C., Champion, J. P., 1998. Spherical Top Data System (STDS) soft-
818 ware for the simulation of spherical top spectra. *Journal of Quantitative*
819 *Spectroscopy and Radiative Transfer* 59, 471–480.
- 820 Wilson, E. H., Atreya, S. K., 2004. Current state of modeling the photochem-
821 istry of Titan's mutually dependent atmosphere and ionosphere. *Journal of*
822 *Geophysical Research (Planets)* 109 (E18), 6002.
- 823 Yelle, R. V., 1991. Non-LTE models of Titan's upper atmosphere. *Astrophys.*
824 *J.* 383, 380–400.
- 825 Yelle, R. V., Griffith, C. A., 2003. HCN fluorescence on Titan. *Icarus* 166,
826 107–115.
- 827 Yelle, R. V., Strobell, D. F., Lellouch, E., Gautier, D., 1997. The Yelle Titan
828 atmosphere engineering models. *ESA Special Publication: Huygens: Science,*
829 *Payload and Mission* 1177, 243.

Table 1
VIMS observations used in this study.

Encounter/Sequence	Cube	IFOV [km]	Phase Angle	# of spectra	Geolocations
T34/S32- GLOBMAP003	1563524168	50	60°	5	60° SE, 65° SE, 70° SE, 75° SE, 80° SE
T34/S32- GLOBMAP003	1563524658	47	60°	6	55° SE, 60° SE, 65° SE, 70° SE, 75° SE, 80° SE
T34/S32- GLOBMAP003	1563525149	45	60°	6	45° SE, 50° SE, 55° SE, 60° SE, 65° SE, 70° SE
T35/S33- CIRSSTARE001	1567269485	70	26°	3	60° SW, 40° SW, 0° W

Integration time was 640 ms in all cases.

Table 2
 CH_4 vibrational levels included in the model.

Group	Level	Energy (cm^{-1})
$V^{7.6}$	ν_4	1310.76
	ν_2	1533.34
	$2\nu_4$	2596.00
$V^{3.3}$	$\nu_2 + \nu_4$	2830.00
	ν_1	2917.00
	ν_3	3018.92
	$2\nu_2$	3062.00
$V^{2.3}$	$3\nu_4$	3870.50
	$\nu_2 + 2\nu_4$	4123.00
	$\nu_1 + \nu_4$	4223.50
	$\nu_3 + \nu_4$	4340.00
	$\nu_2 + \nu_3$	4540.00
$V^{1.7}$	$4\nu_4$	5161.10
	$\nu_3 + 2\nu_4$	5588.00
	$\nu_1 + \nu_2 + \nu_4$	5775.00
	$\nu_2 + \nu_3 + \nu_4$	5861.00
$V^{7.6, \text{iso}=2}$	$2\nu_3$	6004.99
	ν_4 (62)	1292.00
$V^{3.3, \text{iso}=2}$	$2\nu_4$ (62)	2588.16
	ν_3 (62)	2999.06

Table 3
CH₄ vibrational bands included in the model.

Group	Upper level	Lower level	$\tilde{\nu}_0$ (cm ⁻¹)	RT [†]
–	ν_2	ν_4	222.58	
7.6 μm	$3\nu_4$	$2\nu_4$	1274.50	
	$2\nu_4$	ν_4	1285.24	RT
	$4\nu_4$	$3\nu_3$	1290.60	
	$\nu_2+2\nu_4$	$\nu_2+\nu_4$	1293.00	
	$\nu_2+\nu_4$	ν_2	1296.66	
	ν_4	ground	1310.76	RT
	$\nu_2+\nu_3+\nu_4$	$\nu_2+\nu_3$	1321.00	
6.5 μm	ν_1	ν_2	1383.66	RT
	ν_3	ν_2	1485.58	
	$\nu_2+\nu_4$	ν_4	1519.24	
3.3 μm	$2\nu_2$	ν_2	1528.66	RT
	ν_2	ground	1533.34	RT
	$\nu_1+\nu_2+\nu_4$	$\nu_1+\nu_4$	1551.50	
	ν_1	ν_4	1606.24	
	ν_3	ν_4	1708.16	
	$2\nu_2$	ν_4	1751.24	
	$3\nu_4$	ν_4	2559.74	
2.3 μm	$4\nu_4$	$2\nu_4$	2565.10	RT
	$2\nu_4$	ground	2614.25	RT, Sun
	$\nu_2+\nu_4$	ground	2838.20	RT, Sun
	$2\nu_3$	ν_3	2986.07	RT, Sun
	ν_1	ground	2916.48	RT
	$\nu_3+2\nu_4$	$2\nu_4$	2992.00	RT, Sun
	$\nu_2+\nu_3$	ν_2	3006.66	RT
	ν_3	ground	3019.49	RT, Sun
	$\nu_3+\nu_4$	ν_4	3029.24	RT
	$\nu_2+\nu_3+\nu_4$	$\nu_2+\nu_4$	3031.00	RT
	$2\nu_2$	ground	3064.39	RT
	$3\nu_4$	ground	3870.00	RT, Sun
	1.7 μm	$\nu_2+2\nu_4$	ground	4123.00
$\nu_1+\nu_4$		ground	4223.50	RT, Sun
$\nu_3+\nu_4$		ground	4340.00	RT, Sun
$\nu_2+\nu_3$		ground	4540.00	RT, Sun
$4\nu_4$		ground	5161.10	
7.6 μm (iso=2)	$\nu_3+2\nu_4$	ground	5588.00	RT, Sun
	$\nu_1+\nu_2+\nu_4$	ground	5775.00	
	$\nu_2+\nu_3+\nu_4$	ground	5861.00	Sun
	$2\nu_3$	ground	6004.99	RT, Sun
3.3 μm (iso=2)	ν_4 (62)	ground	1292.00	RT
	$2\nu_4$ (62)	ν_4	1296.16	RT
3.3 μm (iso=2)	$2\nu_4$ (62)	ground	2588.16	RT
	ν_3 (62)	ground	2999.06	RT

[†] Radiative transfer. RT: full radiative transfer among atmospheric layers included. Sun: The absorption of solar radiation in this band is important (i.e., $A_{21} \gg l_t$, where A_{21} is Einstein coefficient for spontaneous emission of the vibration-rotation band and l_t is specific loss of the upper level of the transition due to collisions).

Table 4
Collisional processes included in the CH₄ model.

No.	Process	Rate (cm ³ s ⁻¹)	Reference
1a	CH ₄ ⁱ (v ₁ , v ₂ , v ₃ , v ₄) + N ₂ ⇌ CH ₄ ⁱ (v ₁ , v ₂ , v ₃ , v ₄ - 1) + N ₂	$k_{VT, N_2} = \exp(-36.82 + 3.27 \times 10^{-3}T + 2.52 \times 10^{-5}T^2)$	Siddles et al. (1994)
1b	CH ₄ ⁱ (v ₁ , v ₂ , v ₃ , v ₄) + CH ₄ ⇌ CH ₄ ⁱ (v ₁ , v ₂ , v ₃ , v ₄ - 1) + CH ₄	$k_{VT, CH_4} = \exp(-37.89 + 3.88 \times 10^{-2}T - 5.85 \times 10^{-5}T^2)$	Siddles et al. (1994)
2a	CH ₄ ⁱ (v ₁ , v ₂ , v ₃ , v ₄) + N ₂ ⇌ CH ₄ ⁱ (v ₁ , v ₂ - 1, v ₃ , v ₄) + N ₂	Same as for process 1a	Siddles et al. (1994)
2b	CH ₄ ⁱ (v ₁ , v ₂ , v ₃ , v ₄) + CH ₄ ⇌ CH ₄ ⁱ (v ₁ , v ₂ - 1, v ₃ , v ₄ - 1) + CH ₄	Same as for process 1a	Siddles et al. (1994)
3a	CH ₄ ⁱ (V _k [*]) + N ₂ ⇌ CH ₄ ⁱ (V _l [*]) + N ₂	$k_{g, N_2} = a \times 10^{-11}$ with: $a = 1, 2, 3, 4$ for $V^* = V^{7.6}, V^{3.3}, V^{2.3}, V^{1.7}$	<i>This work</i> (see text)
3b	CH ₄ ⁱ (V _k [*]) + CH ₄ ⇌ CH ₄ ⁱ (V _l [*]) + CH ₄	$k_{g, CH_4} = b \times 10^{-11}$ with: $b = 0.8, 2.1, 1.8$ for $V^* = V^{3.3}, V^{2.3}, V^{1.7}$	Hess et al. (1980)
	Redistribution of (v ₁ or v ₃) to (2v ₂ or 2v ₄) quanta		
	Redistribution of v ₃ to v ₁ quanta	$k_{g, CH_4} = 3.6 \times 10^{-11}$	Hess et al. (1980)
	Redistribution of v ₂ to v ₄ quanta	$k_{g, CH_4} = 3 \times 10^{-11}$	Hess et al. (1980)
4	CH ₄ ⁱ (v ₁ , v ₂ , v ₃ , v ₄) + CH ₄ ^j ⇌ CH ₄ ⁱ (v ₁ , v ₂ , v ₃ , v ₄ - 1) + CH ₄ ^j (0, 0, 0, 1)	$k_{vv4} = 4.1 \times 10^{-11}$	Avrarides and Hunter (1983)
5	CH ₄ ⁱ (v ₁ , v ₂ , v ₃ , v ₄) + CH ₄ ^j ⇌ CH ₄ ⁱ (v ₁ , v ₂ - 1, v ₃ , v ₄) + CH ₄ ^j (0, 1, 0, 0)	$k_{vv2} = k_{vv4}$	<i>This work</i> (see text)
6	CH ₄ ⁱ (v ₁ , v ₂ , v ₃ , v ₄) + CH ₄ ^j ⇌ CH ₄ ⁱ (v ₁ , v ₂ , v ₃ - 1, v ₄) + CH ₄ ^j (0, 0, 1, 0)	$k_{vv3} = 8 \times 10^{-12}$ if $i=j$ and $v_1=v_2=v_4=0$	(Hess et al., 1980)
		$k_{vv3iso} = 2.5 \times 10^{-12}$ if $i \neq j$	(Hess et al., 1980)
		$k_{vv34} = 6 \times 10^{-12}$ for the rest	(Hess et al., 1980)

i and *j* refer to CH₄ isotopes. *k* and *l* refer to two levels of the same group (see Table 2).

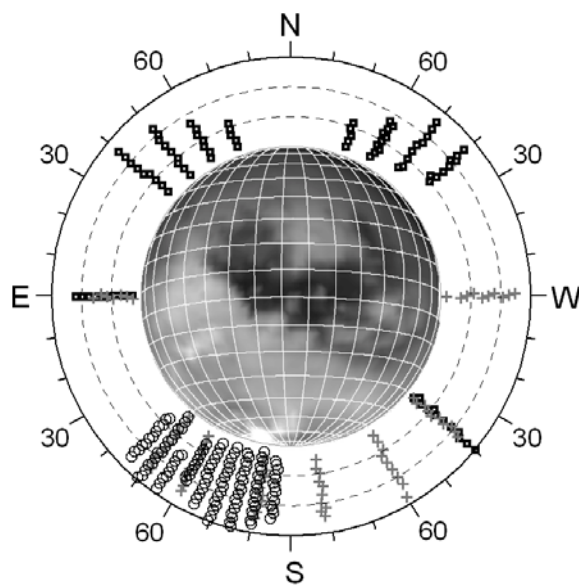


Fig. 1. Section of Titan's atmosphere showing the geolocations and the vertical distribution of the spectral mapping cubes listed in Table 1. The observations refer to the TA (open squares), T34 (open circles) and T35 (grey crosses) Titan encounters. The view of Titan in the center corresponds to encounter TA, representing the Titan opposite side with respect to the prime meridian one. Tangent altitudes (grey dashed lines) are plotted every 500 km.

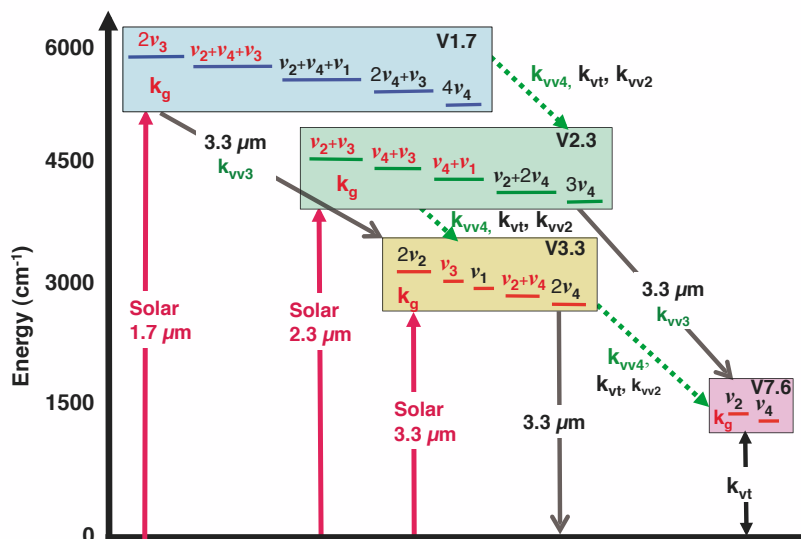


Fig. 2. Diagram of the main isotope CH_4 vibrational energy levels and groups of levels used in the model. The collisions connecting them and the most significant solar absorption bands are also indicated.

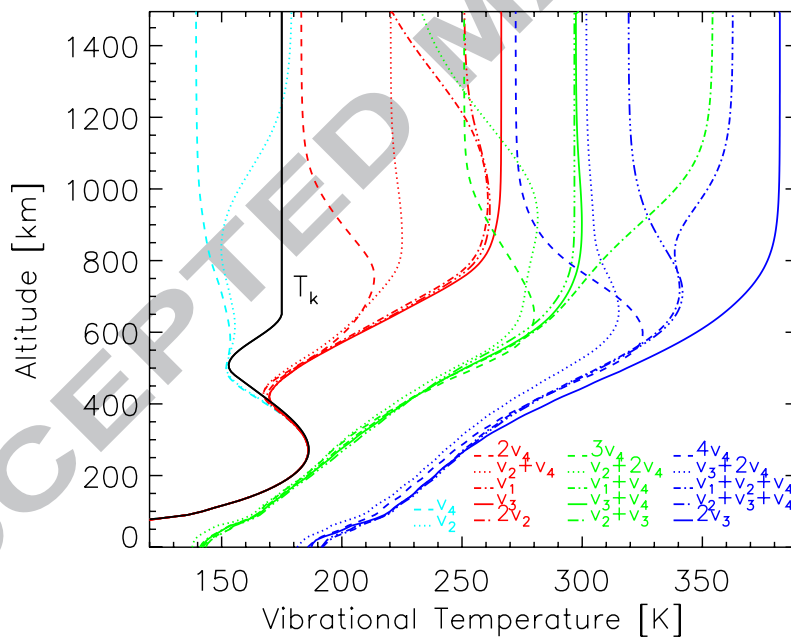


Fig. 3. Nominal vibrational temperatures of the main isotope levels of CH_4 for the YH-atmosphere (see text) and $\text{SZA}=60^\circ$. Kinetic temperature is shown in black.

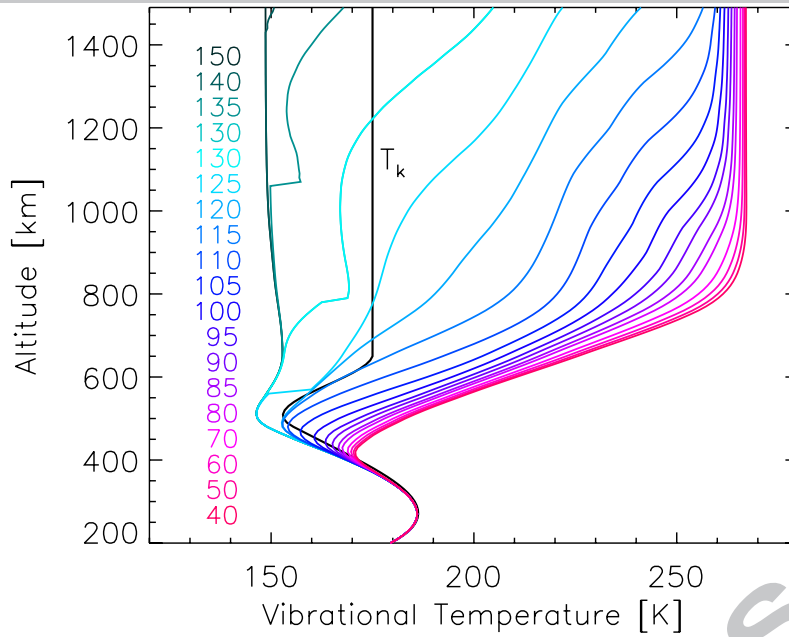


Fig. 4. Vibrational temperatures for the ν_3 level for different solar zenith angles (colors correspond to the values shown in the legend). Kinetic temperature is shown in black.

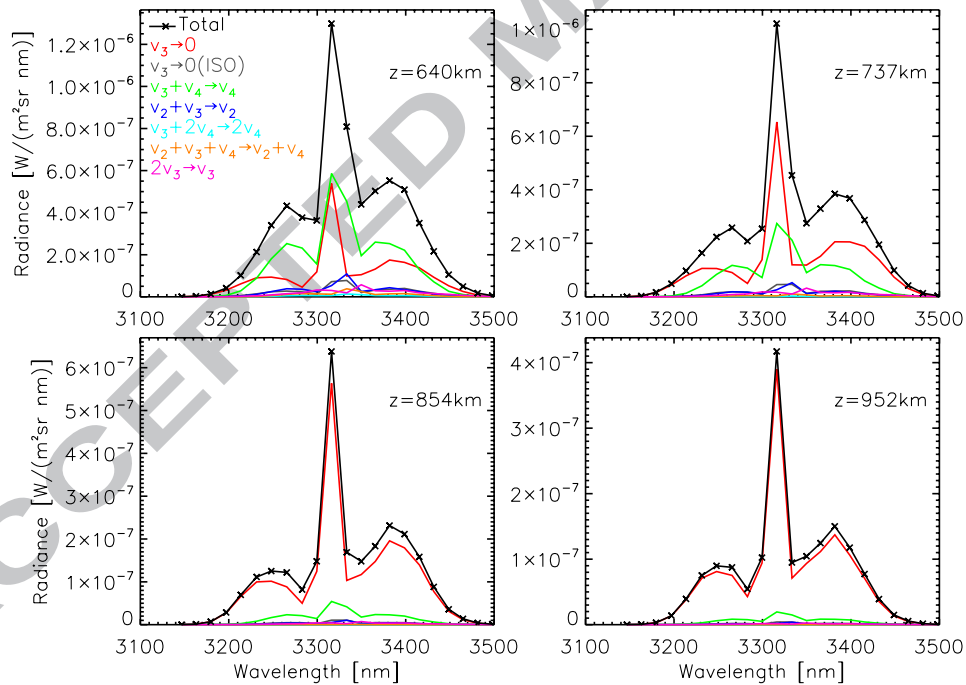


Fig. 5. Titan CH_4 limb simulated spectra around $3.3\ \mu\text{m}$ at the tangent height shown. The contribution of each band (colors) as well as the total (black) are plotted.

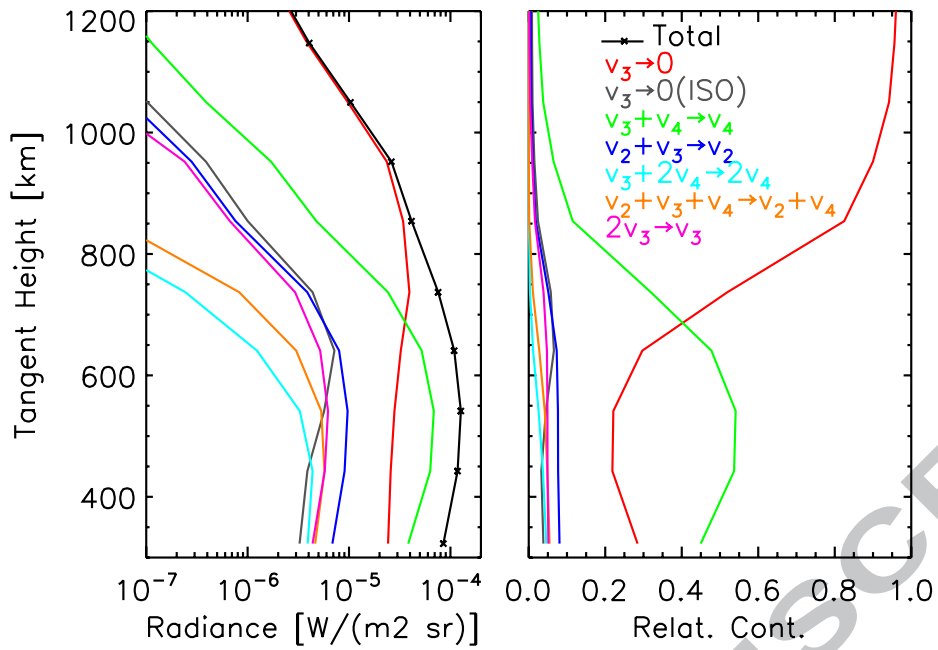


Fig. 6. Left: Integrated radiance of main CH₄ bands emitting at 3.3 μm . Colors are the same as in Fig. 5. Right: Relative contribution of CH₄ bands to total radiance.

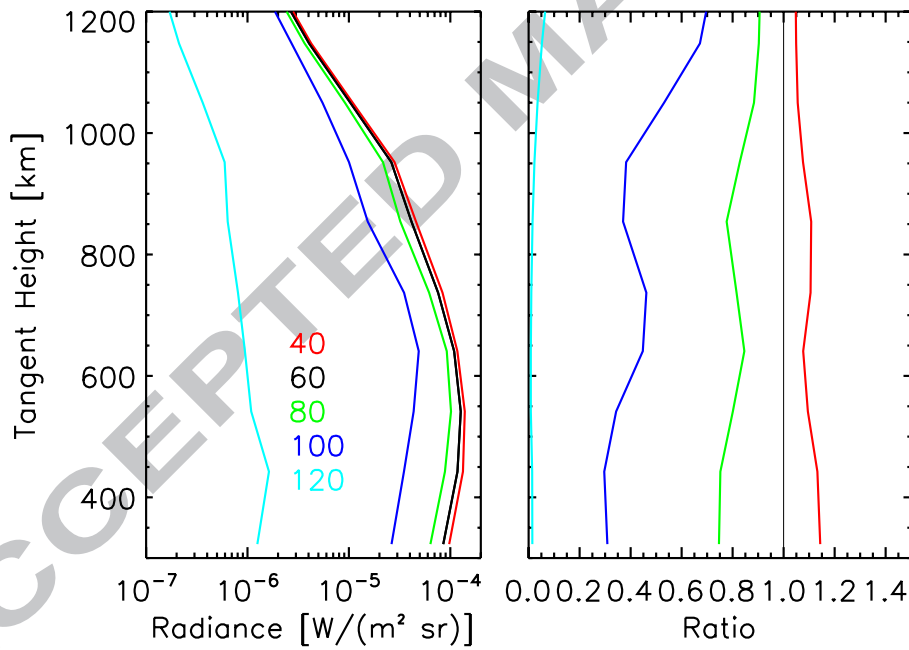


Fig. 7. Dependence of the CH₄ 3.3 μm band integrated radiance on solar zenith angle (Left: Profiles for the solar zenith angles indicated in colors; Right: Ratio of each profile with respect to that corresponding to SZA=60°.)

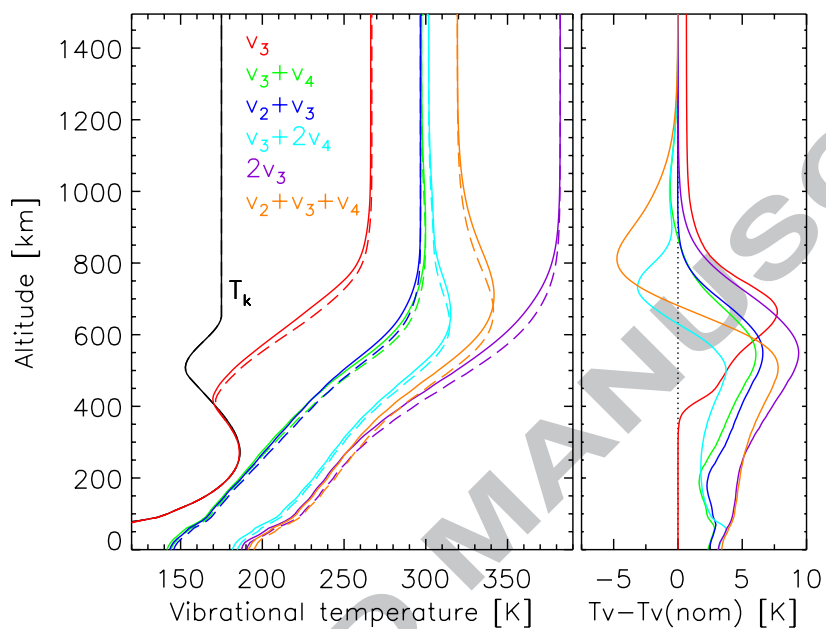


Fig. 8. Effect of k_{g,N_2} on the CH_4 vibrational temperatures of the main $3.3 \mu\text{m}$ emitting levels at $\text{SZA}=60^\circ$. Solid: Nominal rate; dashed: Rate from Doyennette et al. (1998) scaled according to the harmonic oscillator law for each group. Kinetic temperature is shown in black.

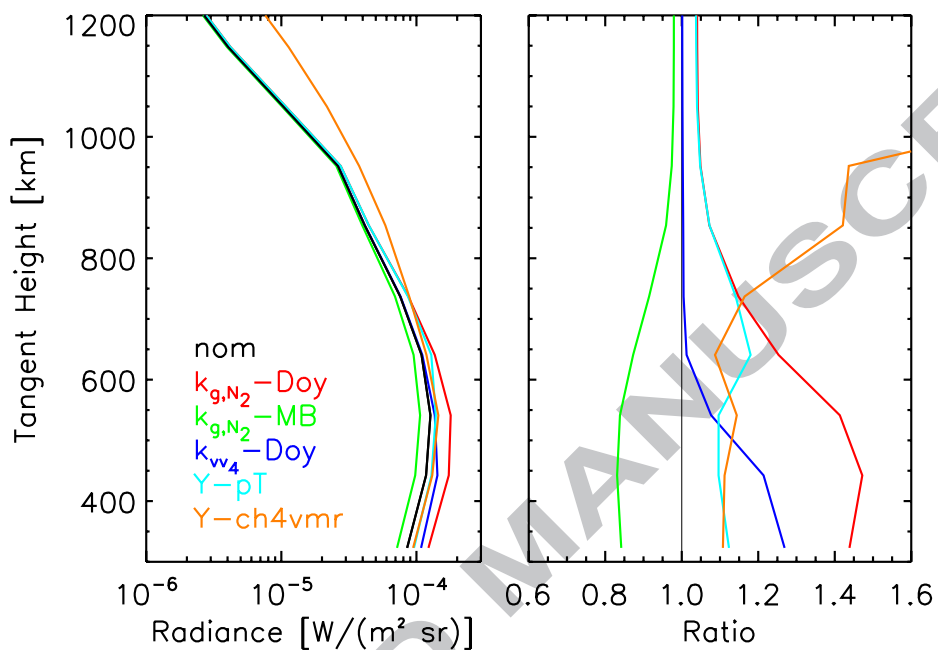


Fig. 9. Left: Effect of using k_{g,N_2} from Doyennette et al. (1998) (red) and from Ménard-Bourcin et al. (2001) (green), k_{vv4} from Doyennette et al. (1998) (dark blue), the Y-atmosphere (light blue), and the Yelle et al. (1997)'s CH_4 volume mixing ratio on the CH_4 $3.3 \mu\text{m}$ band integrated radiance at $\text{SZA}=60^\circ$ (black). Right: Ratio with respect to the nominal radiance.

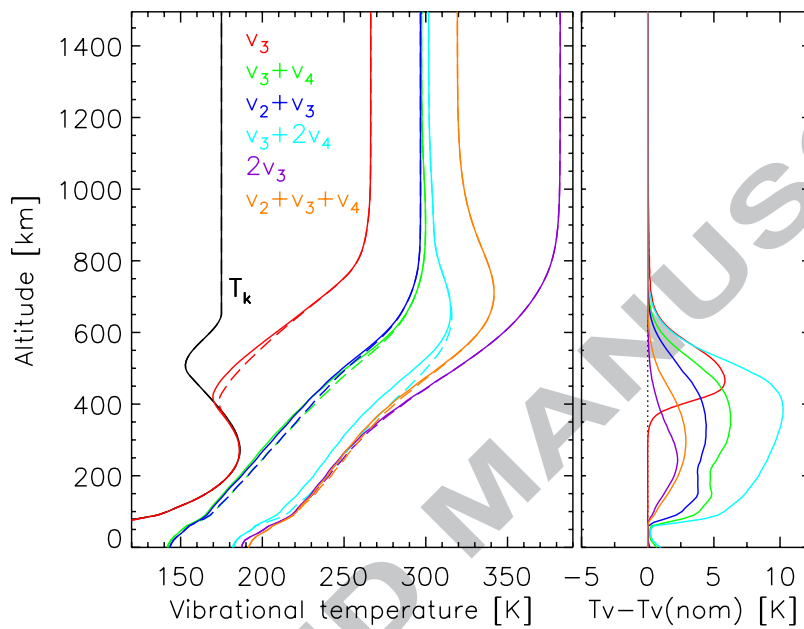


Fig. 10. Effect of k_{vv4} on the CH_4 vibrational temperatures of the main $3.3 \mu\text{m}$ emitting levels at $\text{SZA}=60^\circ$. Solid: Nominal rate (Avramides and Hunter, 1983); dashed: Rate from Doyennette et al. (1998). Kinetic temperature is shown in black.

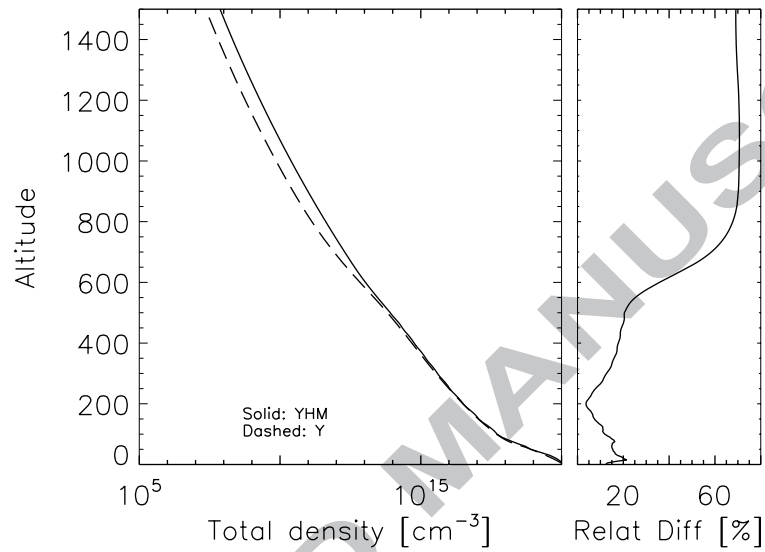


Fig. 11. Comparison of the total number density of the Yelle-HASI (YH) atmosphere (solid) and the Yelle (Y) atmosphere (dashed). Their relative difference (YH–Y) is shown in the right panel.

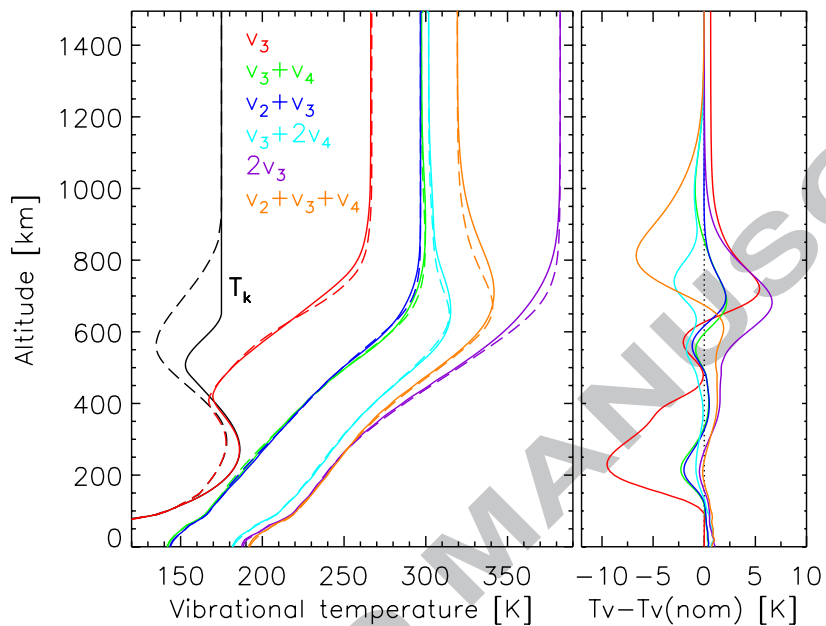


Fig. 12. Sensitivity of the vibrational temperatures of the main $3.3 \mu\text{m}$ CH_4 emitting vibrational levels (see labels) for $\text{SZA}=60^\circ$ to the pressure-temperature structure (solid: YH- atmosphere; dashed: Y-atmosphere). The black lines show the corresponding kinetic temperature profiles.

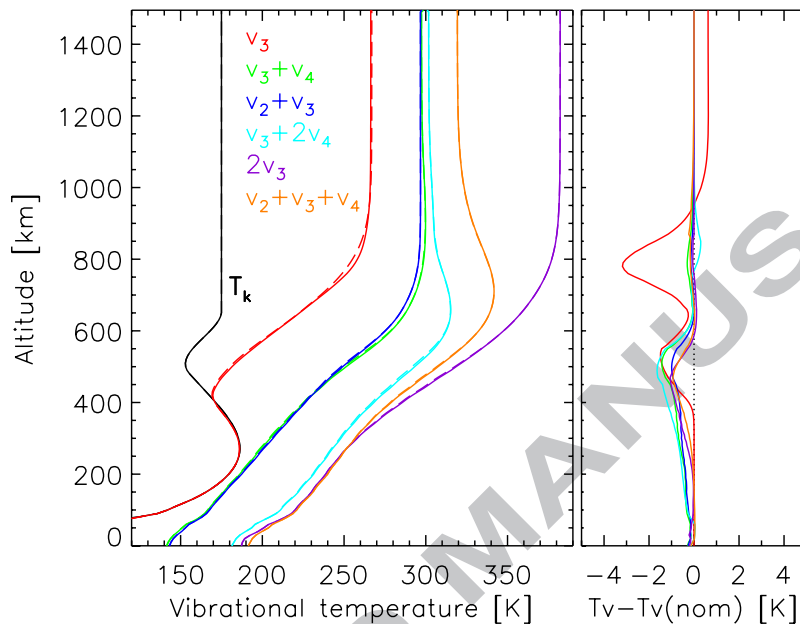


Fig. 13. Sensitivity of the CH_4 vibrational temperatures of the main $3.3 \mu\text{m}$ emitting levels to the CH_4 abundance at $\text{SZA}=60^\circ$ (solid: this work extended with INMS above 1050 km CH_4 vmr; dashed: Yelle recommended CH_4 vmr merged to a constant value below 650 km; see Fig. 17).

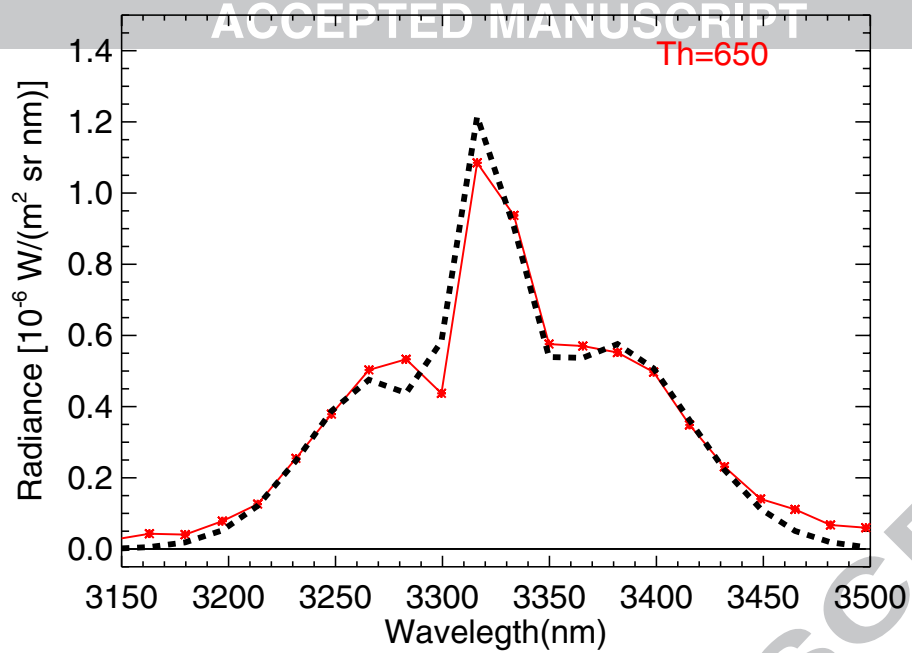


Fig. 14. VIMS mean daytime spectrum (red line) and methane simulated radiance (dashed) in the $3.3 \mu\text{m}$ region at 650 km. The simulated spectrum fits the measurements in the complete CH_4 band at this tangent height.

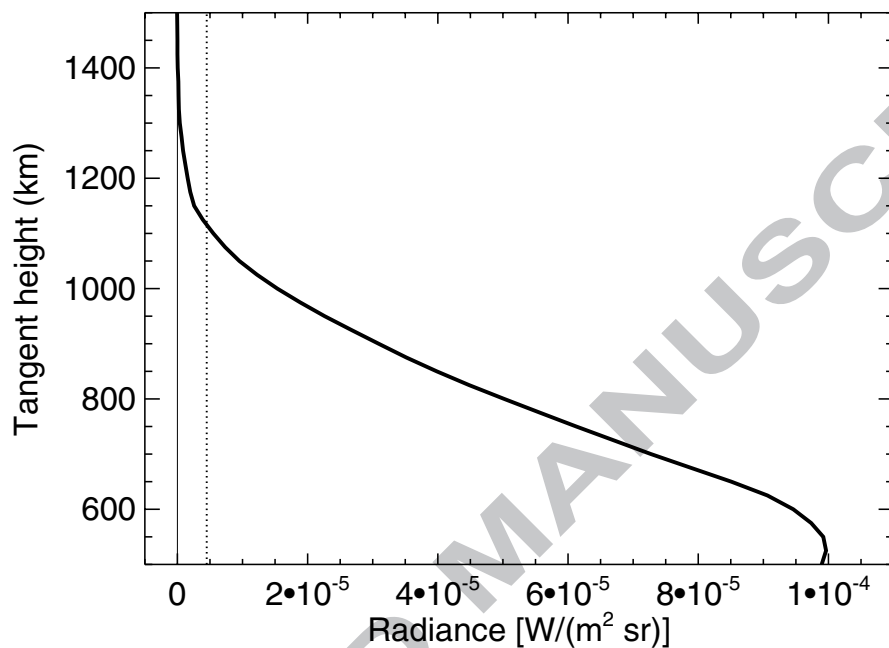


Fig. 15. Mean VIMS integrated radiances in the spectral intervals covering approximately the spectral region from 3300 to 3450 nm (P- and Q-branches). The radiances are the average of 20 measured profiles. The SZAs of the individual profiles vary from around 42° to 70°. Noise error of a single profile is also shown (dotted line).

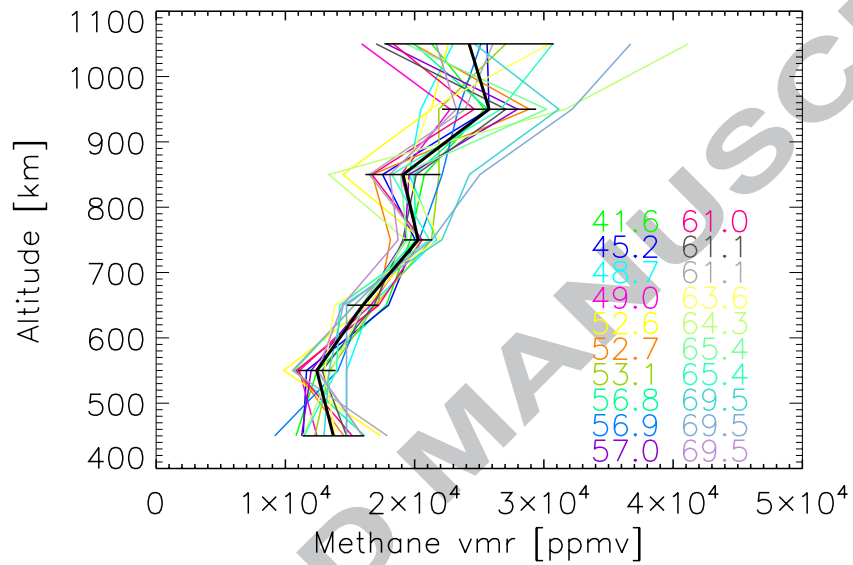


Fig. 16. Methane volume mixing ratio retrieved from VIMS measurements taken at the solar zenith angles indicated by different colors. The black thick line shows the mean profile and the horizontal bars show its standard deviation.

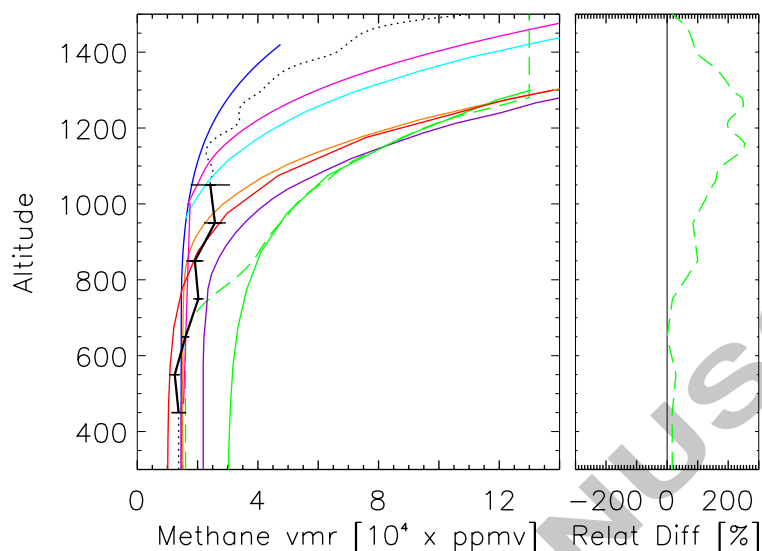


Fig. 17. The black line shows the average CH_4 volume volume mixing ratio derived in this work (solid) extended with Cassini-INMS measurements above 1050 km (dotted). Horizontal bars show the standard deviation of the average. Also shown are the CH_4 vmr from the updated Lara et al. (1996) (dark blue), the Wilson and Atreya (2004) (purple), the Krasnopolsky (2009) (orange), the Müller-Wodarg et al. (2008) (light blue), and the recommended (solid-green) and maximum (red) Yelle et al. (1997) models. The recommended Yelle et al. (1997) CH_4 vmr profile merged with a constant CH_4 below 650 km (dashed-green line) used for our sensitivity studies is also shown. The relative difference between the latter and the profile derived in this work (black line) is shown in the right panel.

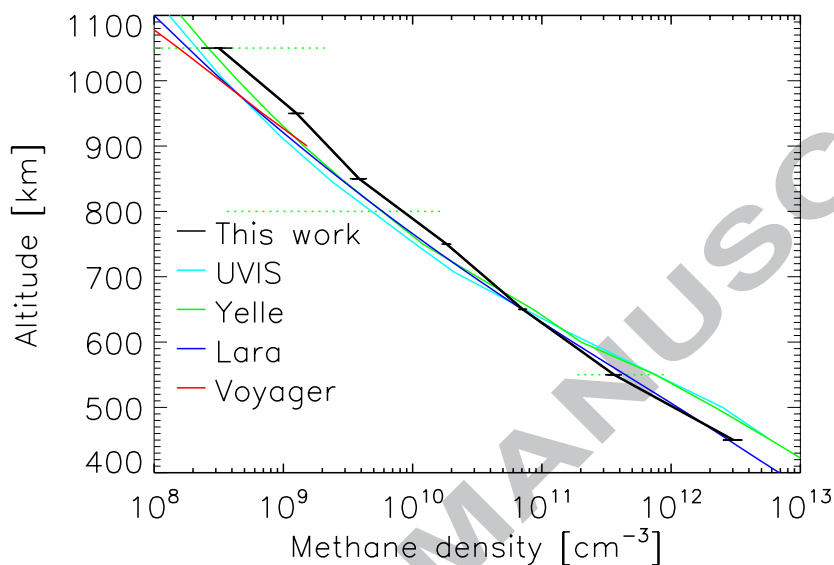


Fig. 18. Comparison of the average methane number density retrieved from VIMS in this work (black) with results from the Yelle's recommended engineering model (Yelle et al., 1997) (green; the horizontal dashed bars indicate the range from their minimum and maximum values), the updated photochemical model of Lara et al. (1996) (dark blue), Voyager measurements (Vervack et al., 2004) (red), and UVIS measurements (Shemansky et al., 2005) (light blue).